The Astrophysical Journal, 745:79 (27pp), 2012 January 20 doi:10.1088/0004-637X/745/1/79
© 2012. The American Astronomical Society. All rights reserved. Printed in the U.S.A.

COLLISIONS BETWEEN GRAVITY-DOMINATED BODIES. I. OUTCOME REGIMES AND SCALING LAWS

Zoë M. Leinhardt[1] and Sarah T. Stewart[2]
[1] School of Physics, H. H. Wills Physics Laboratory, University of Bristol, Tyndall Avenue, Bristol BS8 1TL, UK; Zoe.Leinhardt@bristol.ac.uk
[2] Department of Earth and Planetary Sciences, Harvard University, 20 Oxford St., Cambridge, MA 02138, USA; sstewart@eps.harvard.edu
Received 2011 September 21; accepted 2011 November 29; published 2011 December 29

ABSTRACT

Collisions are the core agent of planet formation. In this work, we derive an analytic description of the dynamical outcome for any collision between gravity-dominated bodies. We conduct high-resolution simulations of collisions between planetesimals; the results are used to isolate the effects of different impact parameters on collision outcome. During growth from planetesimals to planets, collision outcomes span multiple regimes: cratering, merging, disruption, super-catastrophic disruption, and hit-and-run events. We derive equations (scaling laws) to demarcate the transition between collision regimes and to describe the size and velocity distributions of the post-collision bodies. The scaling laws are used to calculate maps of collision outcomes as a function of mass ratio, impact angle, and impact velocity, and we discuss the implications of the probability of each collision regime during planet formation. Collision outcomes are described in terms of the impact conditions and the catastrophic disruption criteria, $Q^*_{\rm RD}$—the specific energy required to disperse half the total colliding mass. All planet formation and collisional evolution studies have assumed that catastrophic disruption follows pure energy scaling; however, we find that catastrophic disruption follows nearly pure momentum scaling. As a result, $Q^*_{\rm RD}$ is strongly dependent on the impact velocity and projectile-to-target mass ratio in addition to the total mass and impact angle. To account for the impact angle, we derive the interacting mass fraction of the projectile; the outcome of a collision is dependent on the kinetic energy of the interacting mass rather than the kinetic energy of the total mass. We also introduce a new material parameter, c^*, that defines the catastrophic disruption criteria between equal-mass bodies in units of the specific gravitational binding energy. For a diverse range of planetesimal compositions and internal structures, c^* has a value of 5 ± 2; whereas for strengthless planets, we find $c^* = 1.9 \pm 0.3$. We refer to the catastrophic disruption criteria for equal-mass bodies as the principal disruption curve, which is used as the reference value in the calculation of $Q^*_{\rm RD}$ for any collision scenario. The analytic collision model presented in this work will significantly improve the physics of collisions in numerical simulations of planet formation and collisional evolution.

Key words: methods: numerical – planets and satellites: formation

Online-only material: color figures

1. INTRODUCTION

Planet formation is common and the number and diversity of planets found increases almost daily (e.g., Borucki et al. 2011; Howard et al. 2011). As a result, planet formation theory is a rapidly evolving area of research. At present, observations principally provide snapshots of either early protoplanetary disks or stable planetary systems. Little direct information is available to connect these two stages of planet formation, therefore, numerical simulations are used to infer the details of possible intermediate stages. However, the diversity of extrasolar planetary systems continues to surprise observers and theorists alike.

A complete model of planet formation has eluded the astrophysics community because of both incomplete physics in numerical simulations and computational constraints. In order to make the problem of planet formation more tractable, the process is often divided into separate stages, which are then tackled in isolation. This method has had some success. For example, *N*-body simulations show that large (∼100 km) planetesimals may grow into protoplanets of about a lunar mass on million year timescales (e.g., Kokubo & Ida 2002). Other simulations, focusing on later stages of planet formation, created a variety of stable planetary systems from initial distributions of protoplanet size bodies (e.g., Chambers 2001; Agnor et al. 1999). Recently, the distribution of stable planets has been investigated in population synthesis models (e.g., Mordasini et al. 2009; Ida & Lin 2010; Schlaufman et al. 2010; Alibert et al. 2011). However, given the complexity of planet formation, it is unsurprising that the predictions from the first population synthesis models have been overturned by the rapidly growing catalog of exoplanets (Howard et al. 2010, 2011). Hence, the diversity of the extrasolar planets is still unexplained.

At the heart of the standard core-accretion model of planet formation is the growth of planetestimals. The evolution of planetesimals is dominated by a series of individual collisions with other planetesimals (e.g., Beauge & Aarseth 1990; Lissauer 1993). The outcome of each collision depends on the specific impact conditions: target size, projectile size, impact parameter, impact velocity, and some internal properties of the target and projectile, such as composition and strength. In the past, direct global simulations of planetesimal evolution have assumed very simplified collision models. In *N*-body simulations, terrestrial planet embryos were shown to grow easily from an annulus of large planetesimals if the only outcome of collisions is merging (e.g., Kokubo & Ida 2002). However, the computational demands of such numerical methods did not allow for the tracking of the very large numbers of bodies necessary to be able to include direct calculations of the erosion of planetesimals.

Statistical methods are required to describe the full population of bodies from dust size to planets. For example, Kenyon & Bromley (2009) conducted simulations that included fragmentation but still relied upon a simple collision model. Specifically, their simulations did not fully account for the effects of the mass

ratio, impact velocity, or impact angle on the collision outcome. In order to overcome these simplifications some previous studies have employed a multi-scale approach that includes direct simulations of collision outcomes within a top-level simulation of planet growth (Leinhardt & Richardson 2005; Leinhardt et al. 2009; Genda et al. 2011a). However, multi-scale calculations significantly increase the computational requirements. In addition, the numerical methods employed in previous studies were only valid for a specific impact velocity regime. In the case of Leinhardt & Richardson (2005) and Leinhardt et al. (2009), the collision model assumed subsonic collisions and could not be extended past oligarchic growth. In the case of Genda et al. (2011a), the technique assumed strengthless bodies and cannot be used in the early phases of planetesimal growth.

A general description of collision outcomes that spans the growth from dust to planets is required to build a self-consistent model for planet formation. In previous work, the description of collision outcomes drew upon a combination of laboratory experiments and limited numerical simulations of collisions between two planetary-scale bodies (see the review by Holsapple et al. 2002). Collision outcomes themselves are quite diverse, and several distinct collision regimes are encountered during planet formation: cratering, merging/accretion, fragmentation/erosion, and hit-and-run encounters.

Individual collision regimes have been described in quite varying detail. In the laboratory, the erosive regimes (cratering and disruption) have been studied most comprehensively (Holsapple 1993; Holsapple et al. 2002); however, even these regimes lack a complete description of the dependence on all impact parameters (particularly mass ratio and impact angle). Recently, numerical studies of collisions between self-gravitating bodies of similar size have identified new types of collision outcomes including hit-and-run and mantle-stripping events (Agnor & Asphaug 2004a; Asphaug et al. 2006, 2010; Marcus et al. 2009, 2010b; Leinhardt et al. 2010; Kokubo & Genda 2010; Benz et al. 2007; Genda et al. 2011b). Up to this point our understanding of these new regimes has not been sufficient to implement the diversity of collision outcomes in planet formation codes. In addition, the transitions between regimes are not clearly demarcated in the literature.

In the work reported here, we present a complete description of collision outcomes for gravity-dominated bodies. Using a combination of published hydrocode and new and published N-body gravity code simulation results, we derive analytic equations to demarcate the transitions between collision regimes and the size and velocity distributions of the post-collision bodies. We describe how these scaling laws can be used to increase the accuracy of numerical simulations of collisional evolution without sacrificing efficiency. In a companion paper (Stewart & Leinhardt 2011), we apply these scaling laws to the end stage of terrestrial planet formation by analyzing the range of collision outcomes from recent N-body simulations.

This paper is organized as follows: Section 2 summarizes the numerical method for the new N-body simulations. Section 3 derives a general catastrophic disruption scaling law. Then, we develop general scaling laws for the size and velocity distributions of fragments in the disruption regime. Section 4 defines the super-catastrophic and hit-and-run regimes. Section 5 presents the transition boundaries between collision outcome regimes from our numerical simulations and our analytic model. Section 6 discusses the range of applicability of our results, areas needing future work, and the implications of the scaling laws on aspects of planet formation. The Appendix summarizes the implementation of the scaling laws in numerical simulations of planet formation and collisional evolution.

2. NUMERICAL METHOD

In this section, we describe the numerical method used in the new impact simulations presented in this work. Simulations of relatively slow subsonic impacts were conducted using an N-body code with finite-sized spherical particles, PKDGRAV (Stadel 2001), which has been extensively used to study the dynamics of collisions between small bodies (e.g., Leinhardt et al. 2000; Michel et al. 2001; Leinhardt & Richardson 2002, 2005; Durda et al. 2004; Leinhardt & Stewart 2009; Leinhardt et al. 2010).

Both the target and projectile are assumed to be rubble piles: gravitational aggregates with no bulk tensile strength (Richardson et al. 2002). The rubble-pile particles are bound together purely by self-gravity. The particles themselves are indestructible and have a fixed mass and radius (for cases without merging). The equations of motion of the particles are governed by gravity and inelastic collisions. The amount of energy lost in each particle–particle collision is parameterized through the normal and tangential coefficients of restitution. The rubble piles are created by placing particles randomly in a spherical cloud and allowing the cloud to gravitationally collapse with highly inelastic particle collisions. Randomizing the internal structure of the rubble piles avoids spurious collision results due to crystalline structure of hexagonal close packing (see Leinhardt et al. 2000; Leinhardt & Richardson 2002). The crystalline structure can cause large uncertainties in collision outcomes for super-catastrophic events.

All simulations had a target with radius of 10 km, mass of 4.2×10^{15} kg, bulk density of 1000 kg m^{-3}, and escape velocity of 7.5 m s^{-1}. The current study includes four projectile-to-target mass ratios (γ), four impact angles (θ), and a range of impact velocities spanning merging to super-catastrophic disruption. These results for a single size target body are used to derive scaling laws for any size body in the gravity regime. The target and projectile are initially separated by the sum of their respective radii to ensure that the impact angle of the impact is unchanged from the initial trajectory.

In order to resolve the size distribution after the collisions, each body needs a relatively high number of particles ($N_{\rm targ} \sim 10^4$, $N_{\rm p} \sim 250$–10^4 depending on the mass ratio). However, large numbers of particles are also time consuming to integrate, especially in a rubble-pile configuration where there is a high frequency of particle–particle collisions. Each simulation here uses high resolution with inelastic particle collisions to resolve the initial impact. Once the velocity field is well established, the particles are allowed to merge with one another. Thus, our method has both accuracy and efficiency, resolving the size distribution to small fragments and completing the simulations as quickly as possible.

We considered the possible influence of the time of the transition from inelastic bouncing to perfect merging. Figure 1 presents a test case using a head-on catastrophic impact between equal-sized objects (mass ratio $\gamma = 1$). Each body has $\sim 10^4$ particles; in the inelastic bouncing phase, each particle has a normal coefficient of restitution, $\epsilon_n = 0.5$, and a tangential coefficient of restitution, $\epsilon_t = 1$, consistent with field observations and friction experiments on rocky materials (e.g., Chau et al. 2002). At a certain time, the colliding particles are al-

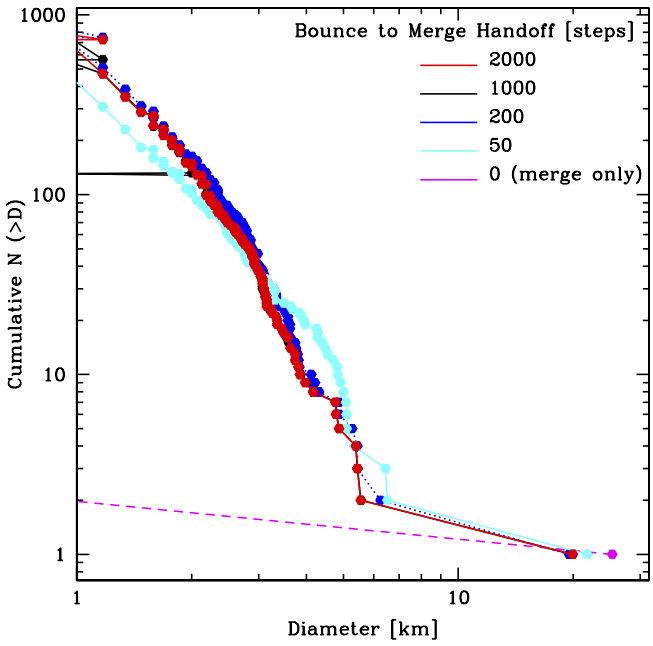

Figure 1. Cumulative size distribution of collisional debris after the catastrophic impact between two 20 km diameter bodies. Line colors represent different handoff times from inelastic bouncing to perfect merging for the outcome of collisions between pairs of PKDGRAV particles. Each step corresponds to 1 minute in simulation time. The same initial impact is used for all distributions shown: $\gamma = 1$, $V_i = 30$ m s^{-1}, $\theta = 0$, $N_{\rm targ} = N_{\rm p} = 1 \times 10^4$.

(A color version of this figure is available in the online journal.)

lowed to merge, producing one particle with the same mass and bulk density as the two original particles. If merging is turned on too early, the mass of the largest remnant is overestimated (magenta and cyan lines) due to a geometric effect known as runaway merging (Leinhardt & Stewart 2009). The results of this numerical test show that the mass distribution is stable if merging is turned on after 50 steps, where one step is one minute in simulation time in the frame of the particles. However, we choose to be conservative and merge after 250 steps of inelastic bouncing in all of the new simulations presented in this paper. All simulations were run for at least 0.2 years, at which point the size distribution had stabilized and clumps of rubble-pile fragments were easily identifiable.

Previous studies using PKDGRAV did not have the numerical resolution to determine an accurate size or velocity distribution of the collisional remnants (e.g., $N_{\rm targ} \sim 10^3$; Leinhardt et al. 2000). In this work, we present more extensive simulations at an order of magnitude higher resolution ($N_{\rm targ} \sim 10^4$). Note that $N = 10^4$ is high resolution for N-body simulations of colliding rubble-pile bodies with bouncing particles. We conducted several resolution tests and find that the random error on the mass of the largest remnant is a few percent of the total system mass. Hence, the super-catastrophic impacts, where the largest remnant mass is a few percent of the total system mass, have the highest error. We achieve excellent reproducibility of the slope of the size and velocity distributions with the nominal resolution compared to the higher resolution tests.

Note that N-body simulations are inherently higher resolution compared to smoothed particle hydrodynamics (SPH) simulations. Our simulations resolve over a decade in fragment size, comparable to SPH simulations using an order of magnitude more particles (Durda et al. 2004). Fragments of radius 0.5 km are considered the smallest usable fragments in these simulations.

In the following sections, we also include published results of subsonic and supersonic collisions from previous work (Leinhardt & Stewart 2009; Agnor & Asphaug 2004a, 2004b; Marcus et al. 2009, 2010b; Durda et al. 2004, 2007; Jutzi et al. 2010; Benz & Asphaug 1999; Benz 2000; Stewart & Leinhardt 2009; Korycansky & Asphaug 2009; Nesvorný et al. 2006; Benz et al. 2007). Studies of supersonic collisions utilize shock physics codes, which include the effects of irreversible shock deformation. For computational efficiency, the shock code is generally used to calculate only the early stages of an impact event; after a few times the shock wave crossing time, the amplitude of the shock decays to the point where further deformation is negligible. After the hydrocode step, the gravitational reaccumulation stage of disruptive events has been calculated directly using PKDGRAV (e.g., Leinhardt & Stewart 2009; Durda et al. 2004; Michel et al. 2002) or indirectly by iteratively solving for the mass bound to the largest fragment (e.g., Benz & Asphaug 1999; Benz 2000; Marcus et al. 2009).

3. RESULTS: THE DISRUPTION REGIME

In our model, the boundaries between collision outcome regimes are defined using the catastrophic disruption criteria, the specific energy required to gravitationally disperse half the total mass, because it provides a convenient means of calculating the mass of the largest remnant. Our definition of the disruption regime refers to collisions in which the energy of the event results in mass loss (fragmentation) between about 10% and 90% of the total mass. More quantitatively, the disruption regime is defined as collision that result in the largest remnant having a linear dependence on the specific impact energy. The rationale for this definition will become apparent in Section 3.1.1.

This section focuses on deriving the dynamical outcome (the mass and velocity distributions of post-collision fragments) in the disruption regime. Other collision regimes are discussed in Section 4. Before discussing the results of our new numerical simulations, we briefly review the catastrophic disruption criterion, as it is a fundamental part of our story.

In the literature on planetary collisions, Q traditionally denotes the specific energy of the impact (kinetic energy of the projectile/target mass) and Q^* indicates the catastrophic disruption criterion, where the largest remnant has half the target mass. Upon recognition that gravitational dispersal was important, Q^*_S and Q^*_D denoted the criteria for shattering in the strength regime and dispersal in the gravity regime, respectively. All of the previous definitions for Q^* assumed that the projectile mass, $M_{\rm p}$, was much smaller than the target mass, $M_{\rm targ}$; however, in several phases of planet formation it is expected that $M_{\rm p} \sim M_{\rm targ}$. Therefore, in previous work, we developed a disruption criterion in the center of mass reference frame in order to study collisions between comparably sized bodies (Stewart & Leinhardt 2009). The subscript R was added in the modification of the specific energy definition to denote reduced mass. The center of mass specific impact energy is given by

$$\begin{aligned} Q_R &= \left(0.5 M_{\rm p} V_{\rm p}^2 + 0.5 M_{\rm targ} V_{\rm targ}^2\right) \big/ M_{\rm tot}, \\ &= 0.5 \mu V_i^2 \big/ M_{\rm tot}, \end{aligned} \quad (1)$$

where $M_{\rm tot} = M_{\rm p} + M_{\rm targ}$, μ is the reduced mass $M_{\rm p} M_{\rm targ}/M_{\rm tot}$, V_i is the impact velocity, and $V_{\rm p}$ and $V_{\rm targ}$ are the speed of the projectile and target with respect to the center of mass,

respectively. At exactly the catastrophic disruption threshold,

$$Q^*_{\rm RD} = 0.5\mu V^{*2}/M_{\rm tot}, \quad (2)$$

where we explicitly define V^* to be the critical impact velocity required to disperse half of the total mass for a specific impact scenario (total mass and mass ratio).

The catastrophic disruption criterion is a strong function of size with two components: a strength regime where the critical specific energy decreases with increasing size and a gravity regime where the critical specific energy increases with increasing size. The transition between regimes occurs between a few 100 m and few km radius, depending on the strength of the bodies (see Figure 2 of Stewart & Leinhardt 2009). A general formula for $Q^*_{\rm RD}$ as a function of size was derived by Housen & Holsapple (1990) using π-scaling theory,

$$Q^*_{\rm RD} = q_s\,(S/\rho_1)^{3\bar{\mu}(\phi+3)/(2\phi+3)}\,R_{C1}^{9\bar{\mu}/(3-2\phi)}\,V^{*(2-3\bar{\mu})} + q_g\,(\rho_1 G)^{3\bar{\mu}/2}\,R_{C1}^{3\bar{\mu}}\,V^{*(2-3\bar{\mu})}, \quad (3)$$

where the first term represents the strength regime and the second the gravity regime. R_{C1} is the spherical radius of the combined projectile and target masses at a density of $\rho_1 \equiv 1000\,{\rm kg\,m^{-3}}$. The variable R_{C1} was introduced by Stewart & Leinhardt (2009) in order to fit and compare the disruption criteria for collisions with different projectile-to-target mass ratios and to account for bodies with different bulk densities (e.g., rock and ice). G is the gravitational constant; q_s and q_g are dimensionless coefficients with values near 1. S is a measure of the material strength in units of Pa $\rm s^{3/(\phi+3)}$, and the remaining variables, ϕ and $\bar{\mu}$, are dimensionless material constants. ϕ is a measure of the strain-rate dependence of the material strength with values ranging from 6 to 9 (e.g., Housen & Holsapple 1990, 1999). $\bar{\mu}$ is a measure of how energy and momentum from the projectile are coupled to the target; $\bar{\mu}$ is constrained to fall between 1/3 for pure momentum scaling and 2/3 for pure energy scaling (Holsapple & Schmidt 1987). Note that the form of Equation (3) assumes that the projectile and target have the same density.

In the strength regime, the largest post-collision remnant is a mechanically intact fragment. The catastrophic disruption criterion decreases with increasing target size because more flaws grow and coalesce during the longer loading duration in larger impact events (e.g., Housen & Holsapple 1999). In the gravity regime, disruption requires both fracturing and gravitational dispersal (Melosh & Ryan 1997; Benz & Asphaug 1999); hence the disruption criterion increases with increasing target size. In this regime, the largest remnant is a gravitational aggregate composed of smaller intact fragments. In both regimes, the disruption criteria increases with impact velocity because more of the impact kinetic energy is dissipated by shock deformation at higher velocities (Housen & Holsapple 1990). This work focuses on the gravity regime; the strength regime will be the subject of future studies.

Both Equations (2) and (3) are satisfied by collisions at exactly the catastrophic disruption threshold. The general formula for catastrophic disruption given by Equation (3) describes a family of curves that depend on size, impact velocity, and material parameters (q_g and $\bar{\mu}$). Most previous work fit the material parameters in Equation (3) to planetary bodies of a particular composition under various assumptions (e.g., a fixed impact velocity). Next (Sections 3.1.2–3.1.4), we present a general method to calculate the values for the disruption energy and critical impact velocity for specific impact scenarios and materials.

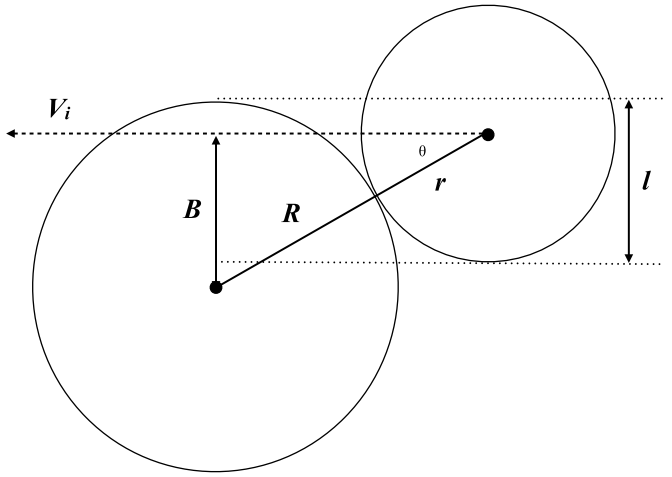

Figure 2. Schematic of the collision geometry. The target is stationary and the projectile is moving from right to left with speed V_i. The impact angle, θ, is defined at the time of first contact as the angle between the line connecting the centers of the two bodies and the normal to the projectile velocity vector. The impact parameter is $b = \sin\theta$.

3.1. Derivation of a General Catastrophic Disruption Law in the Gravity Regime

3.1.1. The Universal Law

In previous work, using simulations of head-on impacts, we determined the value of $Q^*_{\rm RD}$ for a particular pair of planetary bodies by fitting the mass of the largest post-collision remnant, $M_{\rm lr}$, as a function of the specific impact energy, Q_R. The simulations held the projectile-to-target mass ratio fixed and varied the impact velocity. For a wide range of target masses, projectile-to-target mass ratios, and critical impact velocities, we found that the mass of the largest remnant is approximated by a single linear relation,

$$M_{\rm lr}/M_{\rm tot} = -0.5(Q_R/Q^*_{\rm RD} - 1) + 0.5, \quad (4)$$

where $Q^*_{\rm RD}$ was fitted to be the specific energy such that $M_{\rm lr} = 0.5M_{\rm tot}$ (Stewart & Leinhardt 2009; Leinhardt & Stewart 2009). We found that a single slope agreed well with results from both laboratory experiments and numerical simulations. Furthermore, the dimensional analysis by Housen & Holsapple (1990) supports the linearity of the largest remnant mass with impact energy near the catastrophic disruption threshold. Hence, we refer to Equation (4) as the "universal law" for the mass of the largest remnant.

However, the most likely collision between two planetary bodies is not a head-on collision; a 45° impact angle is most probable (Shoemaker 1962). The impact parameter is given by $b = \sin\theta$, where θ is the angle between the centers of the bodies and the velocity vector at the time of contact (Figure 2). The impact parameter has a significant effect on the collision outcome because the energy of the projectile may not completely intersect the target when the impact is oblique. For example, in the collision geometry shown in Figure 2, the top of the projectile does not directly hit the target (above the dotted line). As a result, a portion of the projectile may shear off and only the kinetic energy of the interacting fraction of the projectile will be involved in disrupting the target. Thus, a higher specific impact

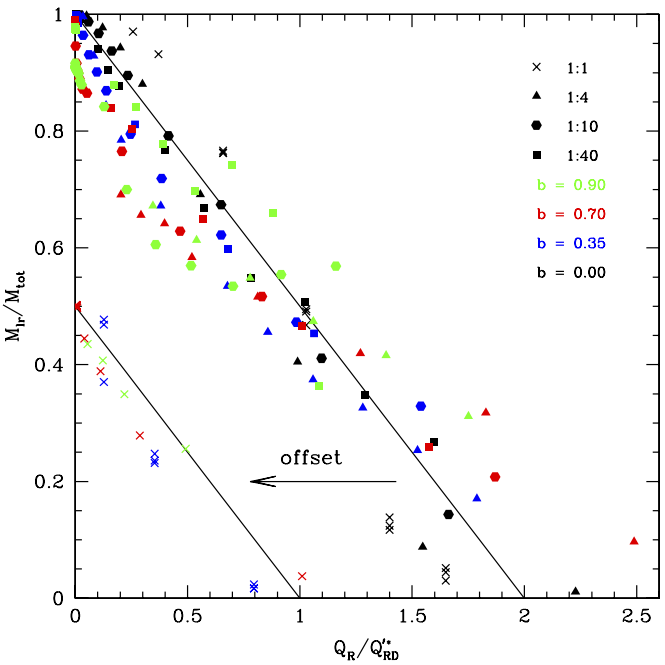

Figure 3. Normalized mass of the largest post-collision remnant vs. normalized impact energy for all collisions in the disruption regime. The impact energy is scaled by the empirical catastrophic disruption criteria Q'^{*}_{RD} (Table 1). The solid lines are the universal law for the mass of the largest remnant (Equation (4)); see the text for discussion of 1:1 oblique impacts. The symbol denotes the projectile-to-target mass ratio, and the color denotes the impact parameter.

(A color version of this figure is available in the online journal.)

energy is required to reach the catastrophic disruption threshold for an oblique impact.

The new PKDGRAV simulations conducted for this study were used to develop a generalized catastrophic disruption law, as previous work did not independently vary critical parameters. Table 1 presents the subset of the simulations discussed in detail below; for a complete listing see Table 4 in the Appendix. The simulations are grouped by impact scenario: fixed mass ratio and impact angle. The value for the catastrophic disruption criterion, $Q'^{*}_{\rm RD}$, is found by fitting a line to the mass of the largest remnant as a function of increasing impact energy in each group. The prime notation in the catastrophic disruption criterion indicates an impact condition that may be oblique ($b > 0$).

With the new data, we first consider how impact angle influences the universal law for the mass of the largest remnant. Figure 3 presents the normalized mass of the largest remnant versus normalized specific impact energy. Our previous simulations (all at $b = 0$) are shown on the same universal law in Stewart & Leinhardt (2009). Note that comparable mass collisions with $b > 0$ need to be considered carefully (offset for emphasis in Figure 3). Such collisions transition from merging to an inelastic bouncing regime (called hit-and-run, discussed in Section 3.1.2) before reaching the disruption regime. As a result, the mass of the largest remnant has a discontinuity between $M_{\rm tot}$ and $M_{\rm targ}$ with increasing impact energy. So, in the case of equal-mass collisions,[3] only the fragments with $M_{\rm lr} < M_{\rm targ}$ are fit by a line of slope -0.5.

Our new results demonstrate that the same universal law for the mass of the largest remnant found for head-on collisions can be generalized to any impact angle:

$$M_{\rm lr}/M_{\rm tot} = -0.5(Q_R/Q'^{\star}_{\rm RD} - 1) + 0.5. \quad (5)$$

In detail, the mass of the largest fragment for a specific subset of simulations may deviate slightly from the universal law (Figure 3). Note that the deviations vary between subsets, with some results systematically sloped more steeply and others sloped more shallowly. The deviations in $M_{\rm lr}/M_{\rm tot}$ from Equation (5) are about 10% for near-normal impacts ($b = 0.00$ and $b = 0.35$) and somewhat larger and more varied for highly oblique impacts.

Overall, the universal law provides an excellent representation for mass of the largest remnant for all disruptive collisions in the gravity regime. As a result, we have chosen to use the range of impact energies that satisfy the universal law for the mass of the largest remnant as the technical definition of the disruption regime. At higher specific impact energies, the linear universal law breaks down in a transition to the super-catastrophic regime ($Q_R/Q^{*}_{\rm RD} \geqslant 1.8$, see Section 4.1). At lower specific impact energies, the outcomes are merging or cratering (Section 5). Using our definition, the disruption regime encompasses less than a factor of two in specific impact energy. The outcomes in the disruption regime span partial accretion of the projectile onto the target to partial erosion of the target body.

Note that the derived values for $Q'^{*}_{\rm RD}$ are strong functions of both the mass ratio and the impact parameter (Table 1). The catastrophic disruption energy rises with smaller projectiles and larger impact parameters. Benz & Asphaug (1999) investigated the effect of impact parameter on the disruption criterion; however, their study fixed the impact velocity and varied the mass ratio of the bodies. Hence, the individual roles of the impact parameter and mass ratio cannot be discerned from their data. In the next two sections, the influence of each factor is isolated and quantified.

3.1.2. Dependence of Disruption on Impact Angle and Derivation of the Interacting Mass

In order to describe the dependence of catastrophic disruption on impact angle, we introduce two geometrical collision groups (Figure 2): *non-grazing*—most of the projectile interacts with the target and *grazing*—less than half the projectile interacts with the target. Following Asphaug (2010), the critical impact parameter,

$$b_{\rm crit} = \left(\frac{R}{R+r}\right), \quad (6)$$

is reached when the center of the projectile (radius r) is tangent to the surface of the target (radius R). Grazing impacts are defined to occur when $b > b_{\rm crit}$.

When considering a non-grazing impact scenario with a particular b and γ, the collision outcome transitions smoothly from merging to disruption as the impact velocity increases. For grazing impacts, however, the collision outcome transitions abruptly from merging ($M_{\rm lr} \sim M_{\rm tot}$) to hit-and-run ($M_{\rm lr} \sim M_{\rm targ}$) and then (less abruptly) to disruption (see Section 5). Thus, only collision energies that result in $M_{\rm lr} < M_{\rm targ}$ should be used in the derivation of $Q'^{*}_{\rm RD}$ in the grazing regime, as done for the $\gamma = 1$ results shown in Figure 3.

During oblique impact events, a significant fraction of the projectile may not actually interact with the target, particularly for comparable mass bodies. For gravity-dominated bodies, the projectile is decapitated and a portion of the mass misses the target entirely. As a result, only a fraction of the projectile's total

[3] A robust fit requires several points between $0.1M_{\rm tot}$ and $M_{\rm targ}$. A similar procedure was applied to fit the $Q'^{*}_{\rm RD}$ for the $b = 0.5$, $\gamma = 1$, and $\gamma = 0.5$ simulations from Marcus et al. (2010b) that are shown in Figure 4.

Table 1
Summary of Parameters and Results from Selected PKDGRAV Simulations (for Full List of Simulations See the Appendix)

$\frac{M_p}{M_{targ}}$	b	V_i	$\frac{M_{lr}}{M_{tot}}$	$\frac{M_{slr}}{M_{tot}}$	β	Q_R	Q'^*_{RD}	α	M_{lr}/M_{tot}	M_{slr}/M_{tot}
	–	(m s^{-1})	M_{tot}	M_{tot}	–	(J kg^{-1})	(J kg^{-1})	–	Predicted	Predicted
1.00	0.00	24	0.76	0.004	4.0	7.2×10^1			0.67	0.01
1.00*	0.00	30	0.50	0.01	3.2	1.1×10^2	1.1×10^2	1	0.49	0.01
1.00	0.00	35	0.12	0.05	2.9	1.5×10^2			0.31	0.02
1.00	0.35	17	0.48	0.46	4.8	3.6×10^1			0.44†	0.44†
1.00	0.35	30	0.23	0.20	3.1	1.1×10^2	5.4×10^1	0.72	0.33†	0.33†
1.00	0.35	45	0.02	0.01	3.7	2.6×10^2			0.11†	0.11†
1.00	0.70	12	0.50	0.49	...	1.8×10^1			0.50†	0.50†
1.00*	0.70	80	0.28	0.27	4.1	8.0×10^2	4.7×10^2	0.22	0.36†	0.36†
1.00	0.70	150	0.04	0.01	3.2	2.8×10^3			super-cat	
1.00	0.90	20	0.50	0.50	...	5.0×10^1			0.50†	0.50†
1.00	0.90	400	0.35	0.34	4.6	2.0×10^4	1.5×10^4	0.03	0.39†	0.39†
1.00	0.90	600	0.25	0.25	3.2	4.5×10^4			0.25†	0.25†
0.25	0.00	30	0.69	0.01	3.7	7.2×10^1			0.72	0.01
0.25†*	0.00	40	0.40	0.02	4.4	1.3×10^2	1.3×10^2	1	0.51	0.01
0.25	0.00	50	0.09	0.02	3.4	2.0×10^2			0.23	0.02
0.25	0.35	30	0.67	0.01	4.5	7.2×10^1			0.81	0.005
0.25*	0.35	40	0.53	0.01	4.1	1.3×10^2	1.9×10^2	0.93	0.66	0.01
0.25	0.35	60	0.25	0.01	3.8	2.9×10^2			0.24	0.02
0.25	0.70	50	0.69	0.01	2.8	2.0×10^2			0.90	0.003
0.25	0.70	100	0.52	0.004	3.3	8.0×10^2	9.9×10^2	0.33	0.60	0.01
0.25	0.70	150	0.32	0.01	2.5	1.8×10^3			0.09	0.02
0.25	0.90	120	0.77	0.14	3.17	1.2×10^3			0.94**	0.002**
0.25	0.90	350	0.47	0.003	4.40	9.9×10^3	9.3×10^3	0.05	0.47	0.01
0.25	0.90	450	0.31	0.01	3.28	1.6×10^4			0.13	0.02
0.10	0.00	40	0.79	0.001	4.9	6.7×10^1			0.79	0.005
0.10	0.00	65	0.41	0.01	3.7	1.8×10^2	1.6×10^2	1	0.45	0.01
0.10	0.00	80	0.14	0.03	3.4	2.7×10^2			0.17	0.02
0.10	0.35	40	0.79	0.002	3.7	6.7×10^1			0.88	0.003
0.10	0.35	80	0.47	0.01	4.5	2.7×10^2	2.7×10^2	1††	0.51	0.01
0.10†*	0.35	100	0.33	0.01	3.6	4.2×10^2			0.23	0.02
0.10*	0.70	100	0.77	0.002	3.6	4.2×10^2			0.90	0.003
0.10	0.70	200	0.52	0.004	3.8	1.7×10^3	2.0×10^3	0.46	0.59	0.01
0.10	0.70	300	0.21	0.01	3.3	3.7×10^3			0.07	0.02
0.10	0.90	400	0.70	0.001	5.2	6.7×10^3			0.89	0.003
0.10	0.90	700	0.53	0.002	4.8	2.0×10^4	2.9×10^4	0.07	0.65	0.01
0.10	0.90	900	0.57	0.01	4.3	3.4×10^4			0.42	0.02
0.025	0.00	100	0.77	0.001	...	1.2×10^2			0.91	0.002
0.025	0.00	140	0.55	0.01	4.45	2.3×10^2	6.4×10^2	1	0.82	0.01
0.025	0.00	160	0.51	0.01	4.10	3.1×10^2			0.76	0.01
0.025	0.35	160	0.60	0.01	3.97	3.1×10^2			0.79	0.01
0.025	0.35	200	0.45	0.01	4.78	4.8×10^2	7.2×10^2	1††	0.67	0.01
0.025	0.35	300	0.07	0.05	3.25	1.1×10^3			0.25	0.02
0.025†*	0.70	300	0.65	0.002	5.08	1.1×10^3			0.73	0.01
0.025	0.70	400	0.47	0.01	3.59	1.9×10^3	2.0×10^3	0.74	0.52	0.01
0.025	0.70	500	0.26	0.01	3.23	3.0×10^3			0.26	0.02
0.025*	0.90	800	0.74	0.001	...	7.7×10^3			0.65	0.01
0.025†*	0.90	900	0.66	0.002	4.06	9.7×10^3	1.1×10^4	0.12	0.56	0.01
0.025	0.90	1000	0.36	0.003	3.77	1.2×10^4			0.46	0.01

Notes. M_p/M_{targ}: mass of projectile normalized by mass of target; b: impact parameter; V_i: projectile impact velocity; M_{lr}/M_{tot}: mass of largest remnant normalized by total mass; M_{slr}: mass of the second largest remnant; β: slope of cummulative size distribution; Q_R: center of mass specific energy; Q'^*_{RD}: empirical critical center of mass specific energy for catastrophic disruption and gravitational dispersal derived from the simulations. In all cases, the target contained $\sim 1 \times 10^4$ particles, $M_{targ} = 4.2 \times 10^{15}$ kg, $R_{targ} = 10^4$ m;
* indicates models shown in blue in Figure 5;
** erosive hit-and-run regime, the disruption regime model does not apply;
† indicates $N_{lr} = 2$ and $N_{slr} = 4$;
†† indicates an α for which $b > 0$ but $l < R$ thus $\alpha = 1$; ... , not enough material to fit a power law;
†* indicates models shown in Figure 7.

kinetic energy is deposited in the target, and the impact velocity must increase to reach the catastrophic disruption threshold.

Using a simple geometric model, we derive the fraction of the projectile mass that is estimated to be involved in the collision. First, we define l as the projected length of the projectile overlapping the target. As shown in Figure 2,

$$l + B = R + r, \tag{7}$$

where $B = (R + r)\sin\theta$. Placing the origin at the bottom of the projectile on the center line and the positive z-axis pointing to the top of the page, the estimated projectile mass involved in the collision, $m_{\rm interact}$, is determined by integrating cylinders of height dz and radius a from 0 to l along the z-axis,

$$m_{\rm interact} = \rho \int_0^l \pi a^2 dz, \tag{8}$$

where ρ is the bulk density of the projectile. The radius of each cylinder can be defined in terms of the radius of the projectile and the height from the origin,

$$a^2 = r^2 - (r - z)^2. \tag{9}$$

Then,

$$m_{\rm interact} = \rho(\pi r l^2 - (\pi/3) l^3). \tag{10}$$

Dividing by the total mass of the projectile, $M_{\rm p}$,

$$\frac{m_{\rm interact}}{M_{\rm p}} = \frac{3rl^2 - l^3}{4r^3} \equiv \alpha. \tag{11}$$

Thus, α is the mass fraction of the projectile estimated to be involved in the collision (see Table 1 for the values of α in our simulations). The entire projectile interacts with the target when $R > b(r + R) + r$; then $l < R$ and $\alpha = 1$.

In order to account for the effect of impact angle on $Q'^*_{\rm RD}$, we include the kinetic energy of only the interacting mass. The appropriate reduced mass is then

$$\mu_\alpha = \frac{\alpha M_{\rm p} M_{\rm targ}}{\alpha M_{\rm p} + M_{\rm targ}}. \tag{12}$$

Now consider the difference between a head-on impact by a projectile of mass $M_{\rm p}$ at V^* and a head-on impact by a projectile of mass $\alpha M_{\rm p}$. At the same impact velocity, the impact energies between the two cases differ by the ratio of the reduced masses,

$$Q'_R = \frac{\mu}{\mu_\alpha} Q_R. \tag{13}$$

Next, in order to conserve the effective specific impact energy, the impact velocity must increase with increasing impact angle such that

$$\bar{V}'^* = \sqrt{\frac{\mu}{\mu_\alpha} V^{*2}}. \tag{14}$$

However, the disruption criterion itself depends on the magnitude of the impact velocity (Equation (3)). In other words, when the effective projectile mass changes, the change in the impact velocity required for disruption varies by more than the factor presented in Equation (14). Combining these two effects leads to the relationship between the oblique and head-on disruption energy for a fixed mass ratio collision,

$$\begin{aligned} Q'^*_{\rm RD} &= \left(\frac{\mu}{\mu_\alpha} Q^*_{\rm RD}\right)\left(\frac{\bar{V}'^*}{V^*}\right)^{2-3\bar{\mu}}, \\ &= \left(\frac{\mu}{\mu_\alpha}\right)^{2-3\bar{\mu}/2} Q^*_{\rm RD}. \end{aligned} \tag{15}$$

By definition, the critical impact velocity for an oblique impact must satisfy Equation (2):

$$V'^* = \sqrt{\frac{2Q'^*_{\rm RD} M_{\rm tot}}{\mu}}. \tag{16}$$

The correction for changing the mass ratio is derived in the next section.

Our model for the effect of impact angle is used to derive equivalent head-on $Q^*_{\rm RD}$ values from our new and previously published catastrophic disruption data. Using the values for $Q'^*_{\rm RD}$ and V'^* fitted to the oblique simulation results, the equivalent head-on impact disruption criteria are

$$Q^*_{\rm RD} = Q'^*_{\rm RD}\left(\frac{\mu}{\mu_\alpha}\right)^{(3\bar{\mu}/2-2)}, \tag{17}$$

$$V^* = \sqrt{\frac{2Q^*_{\rm RD} M_{\rm tot}}{\mu}}. \tag{18}$$

We considered the catastrophic disruption of a wide variety of planetary bodies from the studies summarized in Table 3. First, we fit the general expression for $Q^*_{\rm RD}$ (Equation (3)[4]) to the (equivalent) head-on disruption data to derive the values of q_g and $\bar{\mu}$ that best describe the entire data set, from planetesimals to planets. The same value for the material parameter $\bar{\mu}$ is used in the angle correction and the fit to Equation (3). A small number of data points were excluded from the global fit, which are discussed in Section 6.2.1. The best-fit values for q_g and $\bar{\mu}$ were found by minimizing the absolute value of the log of the fractional error, $\delta = |\log(Q^*_{\rm RD,sim}/Q^*_{\rm RD,model})|$.

In some cases, the impact angle correction is significant (e.g., the impact scenarios with small values of α given in Table 1). With the exception of the constant-velocity results from Benz & Asphaug (1999) and Jutzi et al. (2010) and the mixed velocity data from Benz (2000), the disruption data were derived from simulations conducted with a constant mass ratio and the critical impact velocity for catastrophic disruption, V'^*, was found by fitting to the universal law. For the simulations described in Table 1, the model correction for impact angle usually yields an impact energy within a factor of two of the simulation results for head-on collisions (e.g., within the linear regime for the mass of the largest remnant). We restricted our fits to cases where $\alpha > 0.5$ to reduce any error contribution from a poor model correction for highly oblique impacts.

The compiled data and best-fit model $Q^*_{\rm RD}$ are presented in Figures 4(A) and (B). The combined data are well fit by $q_g = 1.0$ and $\bar{\mu} = 0.35$ ($\delta = 0.14$). Note the good match in the values for V^* (colors) from the simulations with the lines of

[4] In the fitting procedure, the strength term is neglected in Equation (3). For the lines plotted in Figure 4, the strength regime parameters are fixed at $\phi = 7$, $S = 2.4$ Pa s$^{0.3}$, and $q_s = 1$ based on the work in Stewart & Leinhardt (2009).

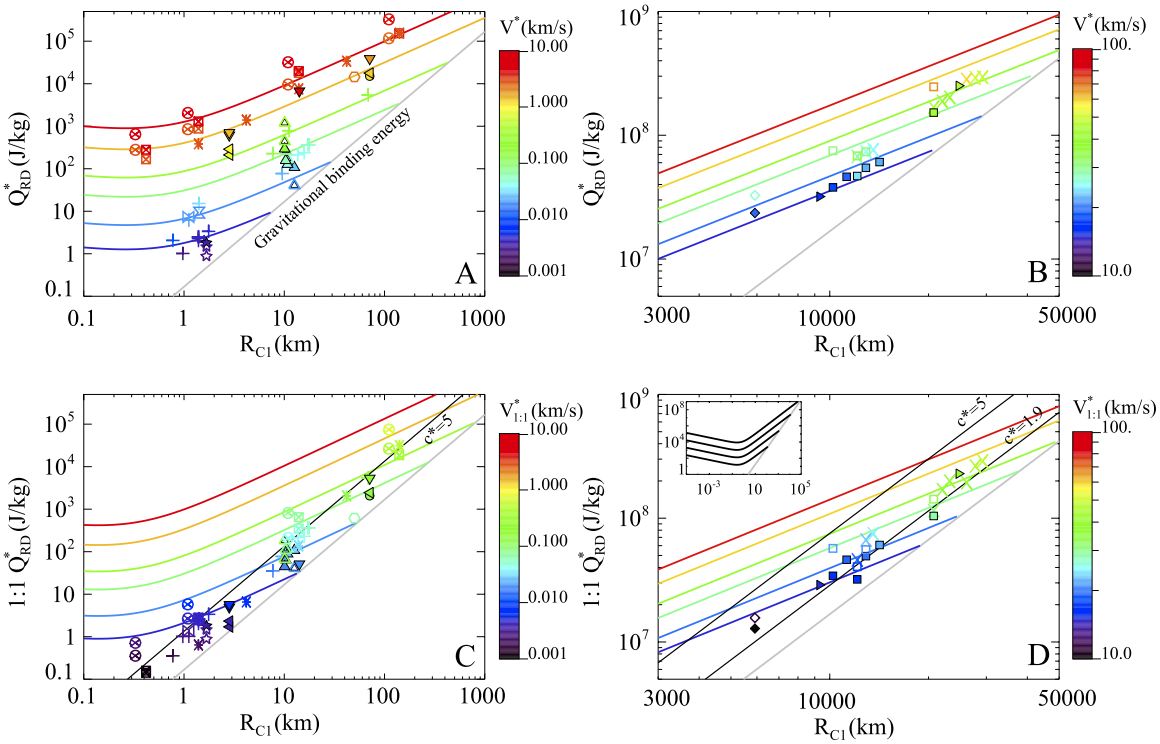

Figure 4. Compilation of gravity-regime catastrophic disruption simulation results. Symbols denote different target materials (Table 3), and color denotes the critical impact velocity, V^*. Filled and line symbols are head-on impacts; open symbols are oblique impacts. (A and B) Data corrected for impact angle to equivalent head-on impact using the interacting mass (Equations (17) and (18)). Constant-velocity $Q^*_{\rm RD}$ curves (Equation (3)) are best fit to all the data with $\bar{\mu} = 0.35$ and $q_g = 1$. The fit between the data and model curves is very good over almost five orders of magnitude in size and nine orders of magnitude in impact energy. Contours for $V^* = .005, .02, .1, .3, 1.5$, and 5 km s^{-1} (A and C) and $V^* = 15, 20, 30, 40, 60$, and 80 km s^{-1} (B and D). (C and D) Data converted to an equivalent equal-mass (1:1) disruption criterion using Equations (23) and (22). The equal-mass data fall on lines proportional to R^2_{C1}. Fits to the equal-mass data are called "principal disruption curves" that are defined by c^* (black lines, Equation (28)); c^* represents the value for the equal-mass $Q^*_{\rm RD}$ in units of the specific gravitational binding energy. Best-fit values are $c^* = 5$ and $\bar{\mu} = 0.37$ for small bodies and $c^* = 1.9$ and $\bar{\mu} = 0.36$ for hydrodynamic planets. Inset: full $Q^*_{\rm RD}$ curves (0.1, 1, 10, 100 km s^{-1}) showing transition from strength to gravity regimes.

(A color version of this figure is available in the online journal.)

constant V^*. Similarly good fits are found for $0.33 \leqslant \bar{\mu} \leqslant 0.36$ and $0.8 \leqslant q_g \leqslant 1.2$ with $0.14 < \delta < 0.15$. Amazingly, the compilation of catastrophic disruption data is well fit by Equation (3) for single values of q_g and $\bar{\mu}$ for a wide variety of target compositions and over almost five orders of magnitude in size and nine orders of magnitude in impact energy. The critical impact velocities span 1 m s^{-1} to several 10's km s^{-1}. The best-fit value for $\bar{\mu}$ falls near pure momentum scaling ($\bar{\mu} = 1/3$).

Upon closer examination, we found that the global fit with Equation (3) systematically predicts a low disruption energy for small bodies ($R_{C1} < 1000$ km) and a high disruption energy for planet-sized bodies. Next, we consider separately the data for small and large bodies. A better fit is found for the small body data in Figure 4(A) with $0.35 \leqslant \bar{\mu} \leqslant 0.37$ and $1.4 \leqslant q_g \leqslant 1.65$ with $0.11 < \delta < 0.12$. The small body data includes hydrodynamic to strong bodies and different compositions. The planet data in Figure 4(B) are best fit with $0.35 \leqslant \bar{\mu} \leqslant 0.375$ and $0.85 \leqslant q_g \leqslant 1.0$ with the very small error of $0.038 < \delta < 0.041$. The planet size data includes three different target compositions. The data for collisions between small strong bodies have the largest dispersion; these data will be discussed in Section 6.2.1.

3.1.3. Dependence of Disruption on Mass Ratio

By fitting such a large collection of data, it is clear that Equation (3) describes a self-consistent family of possible $Q^*_{\rm RD}$ values. For a specific impact scenario, the correct value for V^* at each R_{C1} is ambiguous because V^* depends on both a material property and the mass ratio. In studies that hold V_i constant and vary the mass ratio, the derived value for the critical impact energy only applies for the corresponding critical mass ratio. As noted in previous work, the critical impact velocity falls dramatically as the mass ratio approaches 1:1 (Benz 2000; Stewart & Leinhardt 2009). As a result, collisions between equal-mass bodies require the smallest impact velocity to reach the catastrophic disruption threshold.

Because a mass ratio of 1:1 defines the lowest disruption energy for a fixed total mass, we derive the disruption criterion for different mass ratios with respect to the equal-mass disruption criterion, $Q^*_{{\rm RD},\gamma=1}$. We begin with the equality between the impact energy and gravity term in the disruption energy (Equation (3)),

$$Q_R = Q^*_{\rm RD},$$
$$\frac{\mu V^{*2}}{2M_{\rm tot}} = q_g\,(\rho_1 G)^{3\bar{\mu}/2}\,R_{C1}^{3\bar{\mu}}\,V^{*(2-3\bar{\mu})}. \quad (19)$$

Note that

$$\mu = M_{\rm p}M_{\rm targ}/(M_{\rm p} + M_{\rm targ}),$$
$$= \frac{\gamma}{\gamma+1}M_{\rm targ}, \quad (20)$$

and

$$M_{\rm tot} = (\gamma+1)M_{\rm targ}. \quad (21)$$

Then, substituting for μ and $M_{\rm tot}$,

$$\frac{(\gamma/(\gamma+1))M_{\rm targ}V^{*2}}{2(\gamma+1)M_{\rm targ}} = q_g\,(\rho_1 G)^{3\bar{\mu}/2}\,R_{C1}^{3\bar{\mu}}V^{*(2-3\bar{\mu})},$$

$$V^* = \left[\frac{2(\gamma+1)^2}{\gamma}q_g\,(\rho_1 G)^{3\bar{\mu}/2}\,R_{C1}^{3\bar{\mu}}\right]^{1/(3\bar{\mu})},$$

$$= \left[\frac{1}{4}\frac{(\gamma+1)^2}{\gamma}\right]^{1/(3\bar{\mu})} V^*_{\gamma=1}. \quad (22)$$

Then, for the same total mass, the relationship between the equal-mass disruption energy and any other mass ratio is determined by the difference in the critical impact velocities,

$$Q^*_{\rm RD} = Q^*_{{\rm RD},\gamma=1}\left(\frac{V^*}{V^*_{\gamma=1}}\right)^{(2-3\bar{\mu})},$$

$$= Q^*_{{\rm RD},\gamma=1}\left(\frac{1}{4}\frac{(\gamma+1)^2}{\gamma}\right)^{2/(3\bar{\mu})-1}. \quad (23)$$

The equations for $Q^*_{{\rm RD},\gamma=1}$ and $V^*_{\gamma=1}$ are given in the next section.

In the compilation of catastrophic disruption data shown in Figures 4(C) and (D), all the $\gamma < 1$ data have been converted to an equivalent equal-mass impact disruption energy and the colors denote $V^*_{\gamma=1}$. For example, the critical disruption energy from head-on PKDGRAV simulations with $\gamma = 0.03$ are a factor of three above the disruption energy for $\gamma = 1$ in Figure 4(A) (parallel sets of + from Stewart & Leinhardt 2009). The data lie on the same line after the correction in Figure 4(C). The correction also brings together data from studies using different numerical methods and vastly different material properties. For example, the high-velocity $Q^*_{\rm RD}$ for strong and weak basalt targets (▼, ◀, ⊗, ⊠) fall on the same line as the PKDGRAV rubble piles after the conversion to an equivalent equal-mass impact. Similarly, studies of the disruption of Mercury (Benz et al. 2007) follow the same curve as disruption of Earth-mass water/rock planets (Marcus et al. 2010b). The general form for the equal-mass disruption criteria is derived in the next section.

3.1.4. The Principal Disruption Curve

In the previous two sections, we calculated the disruption criterion for head-on equal-mass collisions by adjusting the critical disruption energy to account for different impact angles and mass ratios. The head-on equal-mass data points, derived from the compilation of numerical simulations, fall along a single curve that we name the "principal disruption curve" (black lines in Figures 4(C) and (D)).

On the principal disruption curve, the critical impact velocity for equal-mass head-on impacts, $V^*_{\gamma=1}$, satisfies both Equation (1) and the gravity regime term in Equation (3):

$$Q_{R,\gamma=1} = Q^*_{{\rm RD},\gamma=1}$$

$$\frac{\mu_{\gamma=1}V^{*2}_{\gamma=1}}{2M_{\rm tot}} = q_g\,(\rho_1 G)^{3\bar{\mu}/2}\,R_{C1}^{3\bar{\mu}}V^{*(2-3\bar{\mu})}_{\gamma=1}. \quad (24)$$

Then, substituting $\mu_{\gamma=1} = M_{\rm targ}/2 = M_{\rm tot}/4$,

$$V^*_{\gamma=1} = \left[8q_g\,(\rho_1 G)^{3\bar{\mu}/2}\,R_{C1}^{3\bar{\mu}}\right]^{1/(3\bar{\mu})},$$

$$= (8q_g)^{1/(3\bar{\mu})}\,(\rho_1 G)^{1/2}\,R_{C1}. \quad (25)$$

Thus, along a curve with a fixed projectile-to-target mass ratio, the critical impact velocity has a linear dependence on R_{C1}. The linear dependence of V^* on R_{C1} for a fixed mass ratio was confirmed by the numerical simulations in Stewart & Leinhardt (2009) (+ in Figure 4).

Then, consider the dependence of the catastrophic disruption criteria on size (Equation (3)) and replace the velocity term with size,

$$Q^*_{{\rm RD},\gamma=1} \propto R_{C1}^{3\bar{\mu}}V^{*(2-3\bar{\mu})},$$

$$\propto R_{C1}^{3\bar{\mu}}R_{C1}^{(2-3\bar{\mu})},$$

$$\propto R_{C1}^2. \quad (26)$$

Thus, the catastrophic disruption criterion scales as radius squared along any curve with a fixed projectile-to-target mass ratio.

Next, note the proximity of the gravity-regime equal-mass disruption energy to the specific gravitational binding energy,

$$U = \frac{3GM_{\rm tot}}{5R_{C1}}, \quad (27)$$

shown as the gray line in Figure 4. We define a dimensionless material parameter, c^*, that represents the offset between the gravitational binding energy and the equal-mass disruption criterion. Then, the principal disruption curve is given by

$$Q^*_{{\rm RD},\gamma=1} = c^*\frac{4}{5}\pi\rho_1 G R_{C1}^2. \quad (28)$$

The parameter c^* is a measure of the dissipation of energy within the target.

The coefficient q_g is found by substituting Equation (2) for $Q^*_{{\rm RD},\gamma=1}$ into Equation (28) and then Equation (25) for $V^*_{\gamma=1}$:

$$\frac{\mu_{\gamma=1}V^{*2}_{\gamma=1}}{2M_{\rm tot}} = c^*\frac{4}{5}\pi\rho_1 G R_{C1}^2,$$

$$(1/8)(8q_g)^{2/(3\bar{\mu})} = c^*\frac{4}{5}\pi,$$

$$q_g = \frac{1}{8}\left(\frac{32\pi c^*}{5}\right)^{3\bar{\mu}/2}. \quad (29)$$

Finally, substituting q_g into Equation (25) gives

$$V^*_{\gamma=1} = \left(\frac{32\pi c^*}{5}\right)^{1/2}(\rho_1 G)^{1/2}R_{C1}. \quad (30)$$

Hence, the critical velocity along the disruption curve for equal-mass impacts is solely a function of R_{C1} and c^*.

The principal disruption curve (Equation (28)) is a simple, yet powerful way to compare the impact energies required to disrupt targets composed of different materials. Each material is defined by a single parameter c^*. In Figures 4(C) and (D), the best-fit values are $c^* = 5 \pm 2$ and $\bar{\mu} = 0.37 \pm 0.01$ for small bodies with a wide variety of material characteristics and $c^* = 1.9 \pm 0.3$ and $\bar{\mu} = 0.36 \pm 0.01$ for the hydrodynamic planet-size bodies. These simulations span pure hydrodynamic targets (no strength), rubble piles, ice, and strong rock targets. Hence, for all the types of bodies encountered during planet formation, c^* is limited to a small range of values. Note that the difference in c^* between the small and large bodies is not simply because of the differentiated structure of the large bodies; two pure rock cases (►, Marcus et al. 2009) fall on the same $Q^*_{{\rm RD},\gamma=1}$ curve. Rather, the large bodies were all studied using

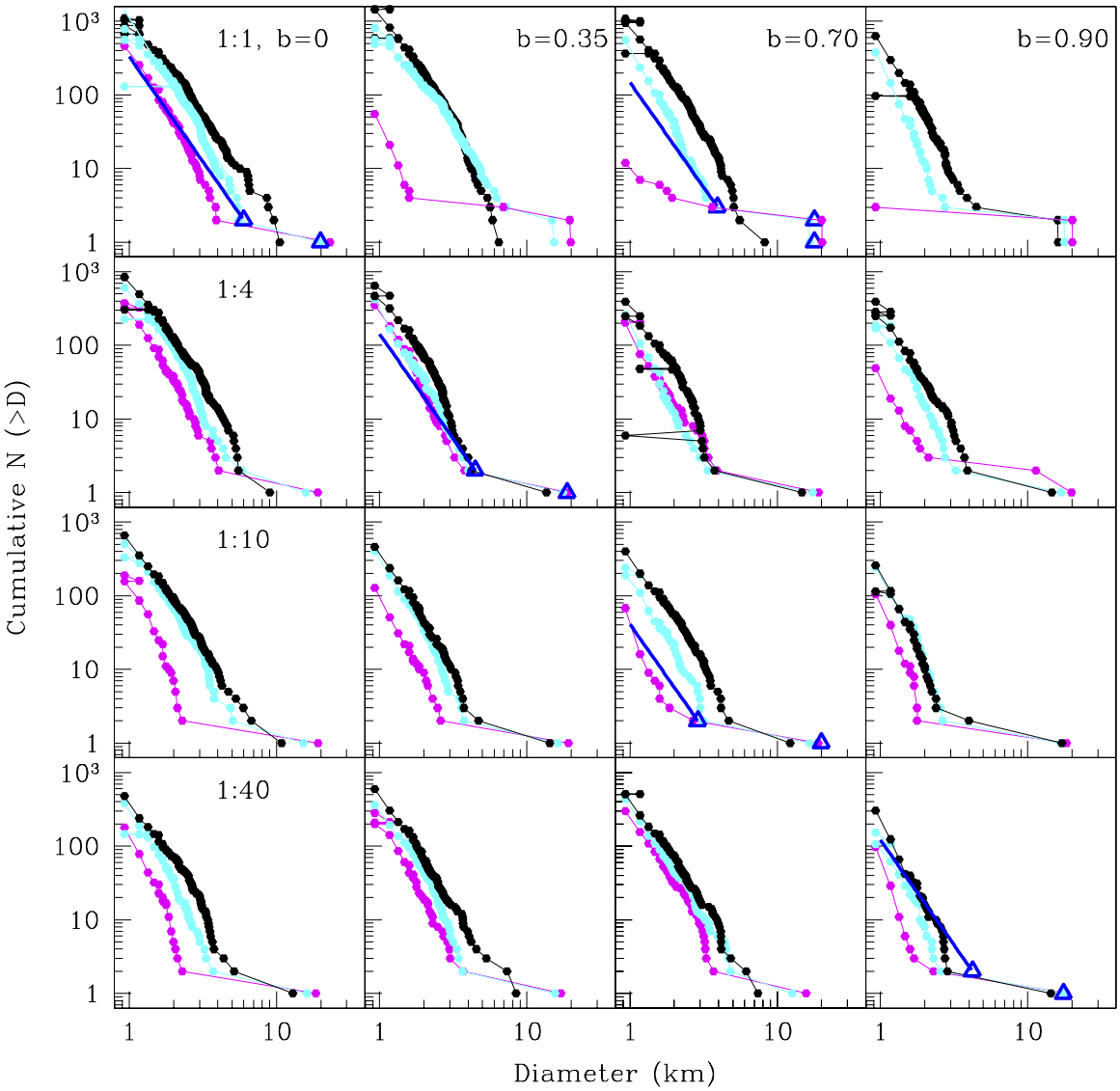

Figure 5. Cumulative size distribution vs. fragment diameter. For each mass ratio γ and impact parameter b, size distributions are shown for three different impact energies. Table 1 provides the details for these simulations. The colors are an aid for the eye: magenta is the lowest energy impact in each block of three in Table 1, black is the highest energy, and cyan is in between. In five panels, the fragment size distribution scaling law (blue line and triangles) is compared to the data. The impact parameters used for the model comparison are indicated in Table 1 by an asterisk "*" in the first column.

(A color version of this figure is available in the online journal.)

a pure hydrodynamic model, whereas the small bodies were studied using techniques that incorporated material strength in various ways. A transition from a higher value for c^* for small bodies to a lower value for planet-sized bodies is appropriate for planet formation studies, as discussed in Section 6.

Now it is clear that most of the differences in the catastrophic disruption threshold found in previous work are the result of differences in impact velocity and mass ratio (few studies varied impact parameter).

Here, we have derived a general formulation for the catastrophic disruption criteria that accounts for material properties, impact velocity, mass ratio, and impact angle. The forward calculation of $Q^*_{\rm RD}$ for a specific impact scenario between bodies with material parameters c^* and $\bar{\mu}$ is described in the Appendix and in the companion paper (Stewart & Leinhardt 2011).

3.2. Fragment Size Distribution

In the disruption regime, our new simulations resolve the size distribution of fragments over a decade in size (Figure 5). In general, the post-collision fragments smaller than the largest remnant form a smooth tail that can be fit well by a single power law. The second-largest remnant forms the base of this tail. For most collisions there is a significant separation in size between the largest and second largest remnants. However, if the collision is very energetic, the largest remnant joins the power-law distribution (e.g., in $\gamma = 1, b = 0.35$). In addition, for the hit-and-run impacts with $\gamma = 1$, the two largest remnants are comparable in size. Only the most energetic scenarios with $\gamma = 1$ fall in the disruption regime (e.g., black lines in $b = 0.35$ and 0.7). In all disruption regime collisions, the slope of the cumulative power-law tail, $-\beta$ (see Table 1), is effectively independent of the impact conditions (b, V_i, γ).

Using the method from Wyatt & Dent (2002) and S. J. Paardekooper et al. (2011, in preparation), the mass of the second largest remnant, $M_{\rm slr}$, is fully constrained by knowledge of the mass/size of the largest remnant and the power-law slope for the size distribution of the smaller fragments. Let us consider

a differential size distribution

$$n(D)dD = CD^{-(\beta+1)}dD, \tag{31}$$

where $n(D)$ is the number of objects with a radius between D and $D + dD$, $-(\beta + 1)$ is the slope of the differential size distribution, and C is the proportionality constant. Integrating Equation (31), the number of bodies between $D_{\rm lr}$ and $D_{\rm slr}$ is

$$N(D_{\rm lr}, D_{\rm slr}) = -\frac{C}{\beta}\left(D_{\rm slr}^{-\beta} - D_{\rm lr}^{-\beta}\right). \tag{32}$$

Therefore, the number of objects larger than the second largest remnant ($D_{\rm slr}$) is $N_{\rm slr} = N(D_{\rm slr}, \infty)$. Assuming that $\beta > 0$,

$$D_{\rm slr} = \left[\frac{N_{\rm slr}}{C}\beta\right]^{\frac{-1}{\beta}}. \tag{33}$$

For spherical bodies with bulk density ρ, the mass of material between $D_{\rm lr}$ and $D_{\rm slr}$ is

$$M(D_{\rm lr}, D_{\rm slr}) = \frac{4}{3}\pi\rho C\frac{D_{\rm slr}^{3-\beta} - D_{\rm lr}^{3-\beta}}{3-\beta}. \tag{34}$$

In order to enforce a negative slope of the remnants, β must be less than 3. Mass is conserved in the impact; thus, the mass in the remnant tail must equal the total mass minus the mass in the largest remnant(s), $M(0, D_{\rm slr}) = M_{\rm tot} - N_{\rm lr}M_{\rm lr}$, where $N_{\rm lr}$ is the number of objects with mass equal to the largest remnant (here, we allow for multiple largest remnants). Substituting for $D_{\rm slr}$ from Equation (33), C is given by

$$\frac{C}{N_{\rm slr}\beta} = \left[\frac{(3-\beta)(M_{\rm tot} - N_{\rm lr}M_{\rm lr})}{(4/3)\pi\rho N_{\rm slr}\beta}\right]^{\frac{\beta}{3}}. \tag{35}$$

Substituting this expression for C into Equation (33) and assuming that all of the objects are spherical, the size and mass of the second largest remnant are expressed in terms of the total mass by

$$\frac{D_{\rm slr}}{D_{\rm tot}} = \left[\frac{(3-\beta)\left(1 - N_{\rm lr}\frac{M_{\rm lr}}{M}\right)}{N_{\rm slr}\beta}\right]^{\frac{1}{3}}, \tag{36}$$

where $D_{\rm tot} = 2((3M_{\rm tot})/(4\pi\rho))^{1/3}$. In the simulations presented here, the calculated diameter of the fragments is not informative because most PKDGRAV particles merge with other particles in gravitationally bound clumps; in these cases, the bulk density is assumed for the size of the merged particle. The mass of the remnants is accurate, however. Rewriting Equation (36) in terms of mass,

$$\frac{M_{\rm slr}}{M_{\rm tot}} = \frac{(3-\beta)\left(1 - N_{\rm lr}\frac{M_{\rm lr}}{M_{\rm tot}}\right)}{N_{\rm slr}\beta}, \tag{37}$$

where $M_{\rm lr}$ is given by the universal law and the catastrophic disruption criteria $Q'^{*}_{\rm RD}$ (Equation (5)).

In the last column of Table 1, the predicted mass of the second largest remnant (Equation (37)) is compared to the numerical simulations using the empirically fit $Q'^{*}_{\rm RD}$, $\beta = 2.85$, $N_{\rm lr} = 1$, and $N_{\rm slr} = 2$. Since the analytic method presented here assumes an infinite size distribution in the fragment tail, we selected the value of β to optimize the fit to the value of $M_{\rm slr}$ in the simulations. This simple method of predicting $M_{\rm slr}$ works well for all impact conditions.[5] To illustrate the model, the predicted size distribution (blue line and triangles) is compared to selected numerical simulation results in Figure 5. In order to predict the size distribution of fragments in the hit-and-run regime impacts between comparable mass bodies ($\gamma = 1$ and $b > 0$), the model needs to be modified slightly. In this special case, we suggest adopting $N_{\rm lr} = 2$ and $N_{\rm slr} = 4$ because the target and projectile each have a nearly identical size distribution of fragments. In this example, the model is calculated for the same impact conditions as the cyan data set with $\gamma = 1$, $b = 0.7$, and $V_i = 80$ m s^{-1} (see Section 4.2 for more detailed discussion of the hit-and-run regime).

The fragment size distributions calculated using our subsonic N-body simulations are consistent with shock code calculations investigating asteroid family formation via catastrophic impact events (Nesvorný et al. 2006; Jutzi et al. 2010). All of the asteroid family-forming simulations used a hybridized numerical technique, combining an SPH code with PKDGRAV in order to model the propagation of the initial shock wave and the subsequent gravitational reaccumulation of the collision remnants. The asteroid family-forming collisions have significantly different impact parameters compared to our simulations: V_i was orders of magnitude larger, γ was an order of magnitude smaller than our smallest γ, and targets were larger (tens of km in diameter). These differences notwithstanding, we find that the range in the values of β for the tail of the size distribution is very similar to our N-body results (note that some published values for β include the largest remnant in the fit, whereas we do not). Qualitatively, we also find a general trend in curvature of the size distribution consistent with Durda et al. (2007), with slightly convex size distributions for super-catastrophic impact events (Section 4.1).

3.3. Fragment Velocity Distribution

Next, we consider the velocity of the collision remnants. The results are easier to interpret by separating the velocities of the largest remnant from the rest of the collision remnants.

We first consider the speed of the largest remnant with respect to the center of mass of the collision (Figure 6). For erosive events ($M_{\rm lr} < M_{\rm targ}$), there is almost no change in the amplitude of the target velocity for impacts with $b = 0.9$. Even at $b = 0.7$, the velocity reduction is minimal for all fractions of mass lost. Because $b = 0.7$ is the center of the probability distribution of impact angles, fully half of all erosive impacts have <10% change in the target velocity amplitude. After head-on collisions ($b = 0$), the largest remnant moves with the center of mass velocity. Note there is significant scatter in the data from $\gamma = 0.025$, which is due to the fact that there was a small number of particles delivering the impact energy to a localized region of the target; thus, the organization of the surface features on both objects becomes important. For disruptive impacts at $b = 0.35$, there is partial velocity reduction of the largest remnant. From these data, we cannot define a unique function for the dependence of $V_{\rm lr}$ on b, and we suggest that a quasi-linear

[5] Because the analytic model for the fragment size distribution assumes an infinite range of sizes in the tail, β is constrained to be less than 3, which is slightly smaller than the slope of power laws that are best fit to the data (Table 1). The fragment size distribution may be modeled under different assumptions, e.g., choosing a minimum diameter in the integral of Equation (31), which would represent the smallest constituent particles or grain size. We have chosen not to impose any assumptions about material properties in the model presented here, but there may be situations where more is known about the colliding bodies and the model for determining $M_{\rm slr}$ and β may be modified.

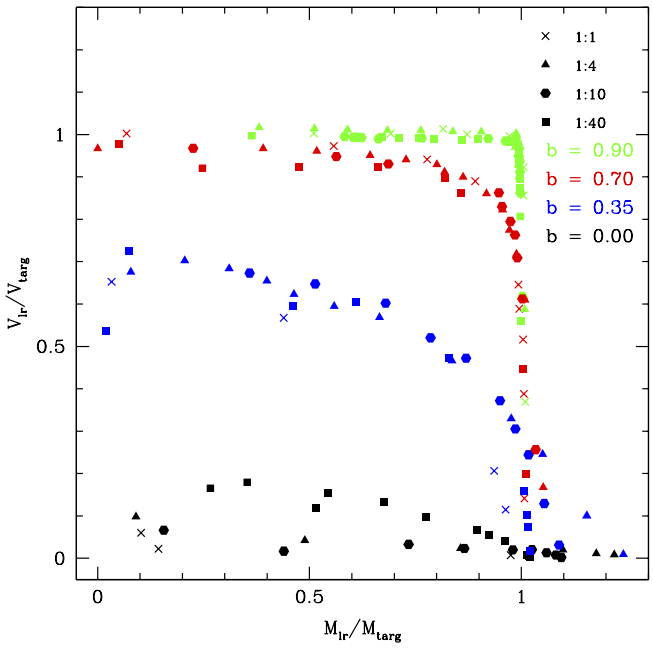

Figure 6. Velocity of largest remnant with respect to the initial center of mass target velocity vs. the mass of largest remnant normalized by the mass of the target. Impact angle is indicated by color; mass ratio is indicated by symbol.

(A color version of this figure is available in the online journal.)

relationship for $0 < b < 0.7$ is a reasonable approximation. We stress that the specific dependence of V_{lr} on b in the disruptive regime is likely to be sensitive to internal structure and composition, so extrapolation of these results beyond weak, constant density objects should be done with caution.

In complete merging events, of course, the post-impact velocity is zero with respect to the center of mass. The $b = 0.35$ data with $M_{lr} > M_{targ}$ steadily approach the center of mass velocity with more mass accreted. The $b = 0.7$ and 0.9 data points plotted near $M_{lr}/M_{targ} = 1$ are primarily hit-and-run events, which will be discussed in Section 4.2.

The smaller remnants of disruptive collisions have a more complex behavior. Figure 7 presents mass histograms of fragments versus velocity with respect to the largest remnant from the simulations summarized in Table 1. The slowest simulations are not plotted for the $\gamma = 0.25$ and 1.0 grazing impacts because there are only a small number of fragments. A significant number of the fragments consist of 10 PKDGRAV particles or less; in Figure 7, mass associated 10 or less particles is shown as dotted histograms. The dotted histograms overlay the total mass histograms for all but the lowest velocity bins; thus, within most of the velocity bins, the simulations do not have the resolution to robustly constrain the size–frequency distribution of the mass in the bin. The smallest (poorly resolved) fragments are found in all velocity bins, while the largest fragments tend to move slowly with respect to the largest remnant. For example, the

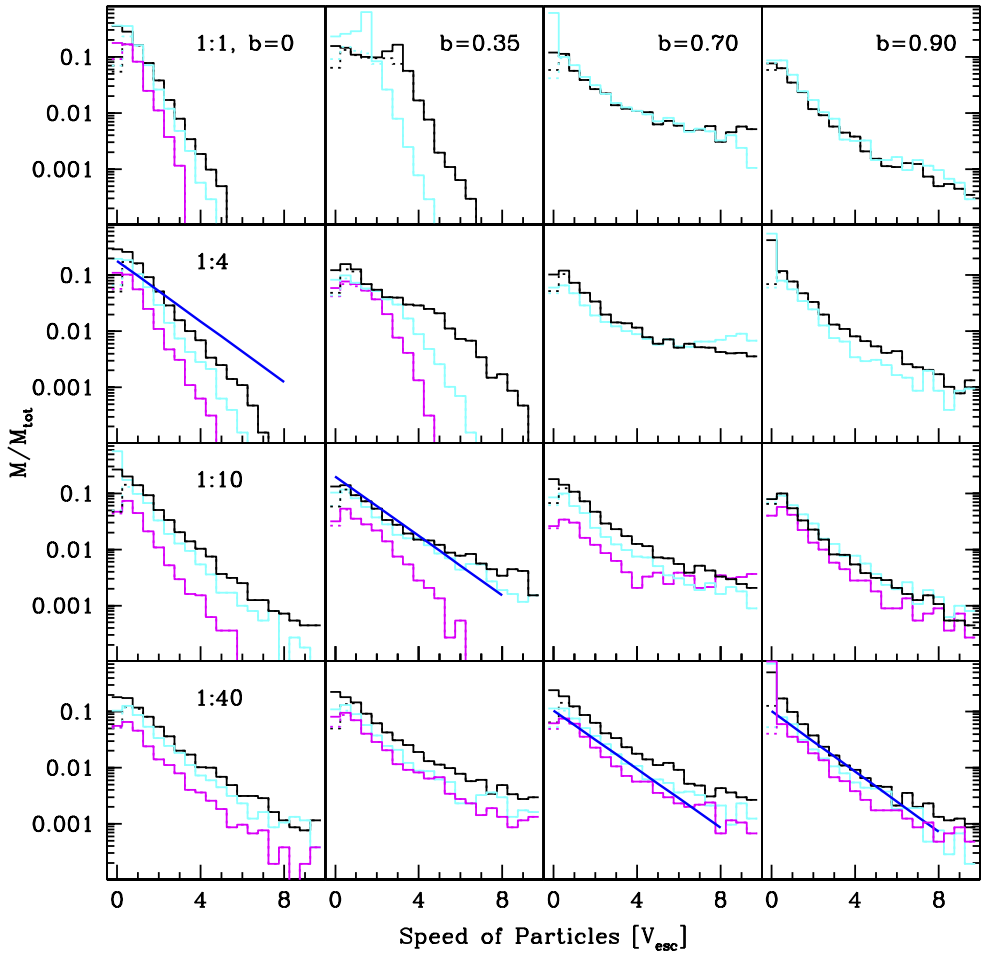

Figure 7. Fragment mass–velocity histograms for simulations in Figure 5 and Table 1. The fragment velocities are relative to the largest remnant in units of the escape velocity from the combined mass of the target and projectile, $V_{esc} = (2GM_{tot}/R_{C1})^{1/2}$. The color coding is the same as in Figure 5. The scaling law predictions are shown in blue.

(A color version of this figure is available in the online journal.)

second largest remnant falls in one of the lowest velocity bins, but that bin is also occupied by smaller fragments.

Hence, to describe the velocity field after a collision, we fit the velocity-binned mass of the collision remnants. The binned mass versus velocity is a fairly well-defined exponential function for most of the simulations. In general, the lowest velocity bin in Figure 7 is of order $0.1 M_{\rm tot}$. Using a least-squares fit of the subset of simulations in Table 1, we find the mass fraction in the lowest velocity bin is proportional to the largest remnant mass:

$$A = -0.3 M_{\rm lr}/M_{\rm tot} + 0.3. \quad (38)$$

To determine the slope, S, of the binned mass versus velocity exponential function, we integrate the differential mass function,

$$\log\left(\Delta v \frac{dm}{dv}\right) = (A - Sv), \quad (39)$$

$$\Delta v \frac{dm}{dv} = 10^{A - Sv}, \quad (40)$$

$$\frac{dm}{dv} = \frac{10^{A-Sv}}{\Delta v} \quad (41)$$

$$\frac{M_{\rm rem}}{M_{\rm tot}} = \int_0^\infty \frac{10^{A-Sv}}{\Delta v} dv, \quad (42)$$

$$S = \frac{10^A}{\ln(10)\,\Delta v\,(M_{\rm rem}/M_{\rm tot})}, \quad (43)$$

where $m = M/M_{\rm tot}$, $v = V/V_{\rm esc}$, Δv is the bin width, and the total mass in the histogram is the total mass in the remaining remnants, $M_{\rm rem} = M_{\rm tot} - M_{\rm lr}$.

The fragment velocity scaling law (Equation (39)) is shown in blue in Figure 7 for selected cases indicated by $^{\dagger *}$ in Table 1. The velocity distributions of the remnants agree qualitatively with those found in hypervelocity simulations of asteroid family-forming events, although previous workers have not fit any function to the velocity distribution of the fragments (e.g., Michel et al. 2002; Nesvorný et al. 2006).

4. OTHER COLLISION REGIMES

4.1. Super-catastrophic Regime

In both laboratory experiments in the strength regime (e.g., Kato et al. 1995; Matsui et al. 1982) and the few high-resolution disruption simulations in the gravity regime (e.g., Korycansky & Asphaug 2009), the relationship between the mass of the largest remnant and the specific impact energy Q_R shows a marked change in slope at around $M_{\rm lr}/M_{\rm tot} \sim 0.1$. We define the super-catastrophic regime when $M_{\rm lr}/M_{\rm tot} < 0.1$ (e.g., when $Q_R/Q'^*_{\rm RD} > 1.8$ by the universal law, Equation (5)). In the super-catastrophic regime, the mass of the largest remnant follows a power law with Q_R rather than the linear universal law.

The slope of the power law for the largest remnant mass versus impact energy shows some scatter in laboratory data, primarily in the range of -1.2 to -1.5. In Figure 8, our few simulations of super-catastrophic collisions (symbols) are compared to the range of outcomes from laboratory experiments (dotted and dashed lines). Based on the simulations in the gravity regime and laboratory experiments in the strength regime, we recommend a power law in the super-catastrophic regime,

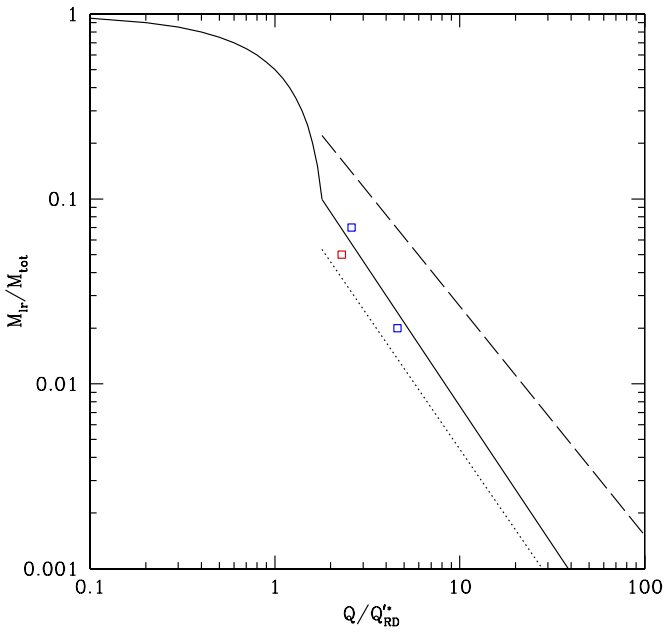

Figure 8. Mass of the largest remnant in the catastrophic and super-catastrophic disruption regimes. The solid line shows the combined universal law (Equation (5)) and recommended power-law relation for $M_{\rm lr}/M_{\rm tot} < 0.1$ (Equation (44)). The symbols are new gravity regime simulations and the dotted and dashed lines represent the range of super-catastrophic disruption data in laboratory experiments in the strength regime. The shape and color of the symbols are the same as in Figure 3.

(A color version of this figure is available in the online journal.)

$$M_{\rm lr}/M_{\rm tot} = \frac{0.1}{1.8^\eta}(Q_R/Q'^*_{\rm RD})^\eta, \quad (44)$$

where $\eta \sim -1.5$ and the coefficient is chosen for continuity with the universal law (Equation (5)). The slope of the power law, about -1.5, is consistent with our gravity regime simulations and a wide range of laboratory experiments summarized in Figure 1 in Holsapple et al. (2002).

In Figure 8, the solid line is the combined universal law and the recommended super-catastrophic power law (Equations (5) and (44)). The dotted line is our fit to disruption data on solid ice from Kato et al. (1992), $M_{\rm lr}/M_{\rm tot} = 0.125(Q_R/Q'^*_{\rm RD})^{-1.45}$. The dashed line is our fit to disruption data on basalt from Fujiwara et al. (1977), $M_{\rm lr}/M_{\rm tot} = 0.457(Q_R/Q'^*_{\rm RD})^{-1.24}$. Note that lab data are available up to very high values of $Q_R/Q'^*_{\rm RD} \sim 100$. The lab data spanning very weak to very strong geologic materials can be considered lower and upper bounds for the parameters in Equation (44).

The general agreement between the gravity and strength regimes suggests that gravitational reaccumulation of fragments has a negligible effect in the super-catastrophic regime. In other words, the mass of the largest fragment is primarily controlled by the shattering process.

Based on the similarity of the size distribution of fragments in laboratory experiments to the gravity regime data presented here (Figure 5), we suggest that the dynamical properties of the smaller fragments in super-catastrophic collisions are similar to the disruption regime. Therefore, the size and velocity distributions described in Sections 3.2 and 3.3 can be applied.

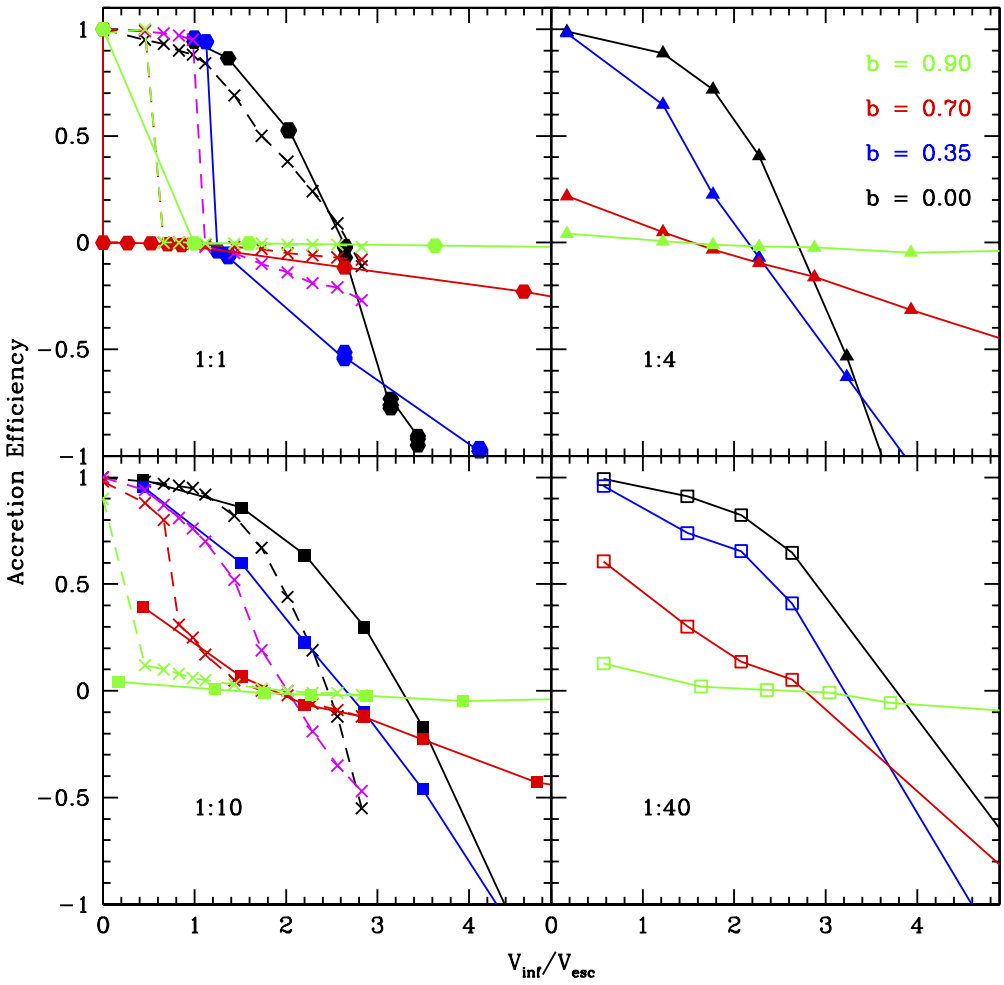

Figure 9. Accretion efficiency (Equation (45)) vs. velocity at infinity normalized by mutual escape velocity for different projectile-to-target mass ratios and impact parameters. Note that the impact velocity $V_i = \sqrt{V_{\rm inf}^2 + V_{\rm esc}^2}$. Results from this work are connected by solid lines; previous results for supersonic impacts between protoplanets are connected by dashed lines (Agnor & Asphaug 2004a, 2004b) and symbols are an aid to differentiate simulation groups. Magenta lines are for $b = 0.5$. (A color version of this figure is available in the online journal.)

4.2. Hit-and-run Regime

Non-grazing impacts in the gravity regime transition from perfect merging to the disruption regime with increasing impact velocity. However, for impact angles greater than a critical value, an intermediate outcome may occur: hit-and-run (Agnor & Asphaug 2004a; Asphaug et al. 2006; Marcus et al. 2009, 2010b; Asphaug 2010; Leinhardt et al. 2010). In a hit-and-run collision, the projectile hits the target at an oblique angle but separates again, leaving the target almost intact. Some material from the topmost layers of the two bodies may be transferred or dispersed. Depending on the exact impact conditions, the projectile may escape largely intact or may sustain significant damage and deformation (e.g., Figure 7 in Asphaug 2010).

The hit-and-run regime is clearly identified by considering the accretion efficiency of a collision, defined by Asphaug (2009) as

$$\xi = \frac{M_{\rm lr} - M_{\rm targ}}{M_{\rm p}}. \quad (45)$$

In a perfect hit-and-run event ($M_{\rm lr} = M_{\rm targ}$), $\xi = 0$. For a perfect accretion event ($M_{\rm lr} = M_{\rm targ} + M_{\rm p}$), $\xi = 1$. An erosive event in which $M_{\rm lr} < M_{\rm targ}$ leads to $\xi < 0$. Note that the negative value of ξ that corresponds to catastrophic disruption ($M_{\rm lr} = 0.5 M_{\rm tot}$) depends on the specific mass ratio of the two bodies ($\xi^* = 0.5$–$0.5/\gamma$).

There is remarkably good agreement in the accretion efficiency and transitions from merging to hit-and-run and from hit-and-run to disruption between this work and previous simulations of higher velocity impacts between large planetary bodies (Agnor & Asphaug 2004a, 2004b; Marcus et al. 2009, 2010b). Figure 9 shows the accretion efficiency from our simulations in solid colored lines for four different projectile-to-target mass ratios and impact parameters. Data for collisions between protoplanets at supersonic velocities from Agnor & Asphaug (2004a, 2004b) (and plotted in Asphaug 2009) are shown in dashed lines for the common mass ratios (1:1 and 1:10). Hit-and-run collisions are indicated by a sudden drop from merging outcomes ($\xi = 1$) to a nearly constant value of $\xi \sim 0$ for a range of impact velocities. Note that the drop in ξ is sharpest for equal-mass bodies. For smaller mass ratios, the transition is not as sharp, and partial accretion of the projectile occurs at energies just above perfect merging (ξ just above 0).

Outcomes that are defined by the disruption regime have steep negative sloped accretion efficiencies. The disruption regime equations apply for partial accretion ($0 < \xi < 1$) and for erosion of the target ($\xi < 0$). Note that for high impact parameters (e.g., $b = 0.7$), there exists an intermediate regime where the

accretion efficiency has a very shallow negative slope and values of ξ just below 0. These impact events, termed erosive hit-and-run, lead to some erosion of the target and more severe deformation of the projectile. The erosive hit-and-run regime is eventually followed by a disruptive style erosive regime at sufficiently high impact velocities. The post-hit-and-run disruptive regime may be identified by finding the impact energy that leads to a linear relationship that satisfies the universal law. The required impact velocity increases substantially with increasing impact parameter; see Section 5 and Marcus et al. (2010b) for an example disruption regime after a hit-and run regime ($\gamma = 0.5$ and $b = 0.5$).

In an ideal hit-and-run event, the target is almost unaffected by the collision, and the velocity of the largest remnant (the target) is about equal to the initial speed of the target with respect to the center of mass. More commonly, there is a small velocity change in both bodies which increases the probability of merging in subsequent encounters (Kokubo & Genda 2010). Agnor & Asphaug (2004a) referred to this collision outcome as inelastic bouncing. In our hit-and-run simulations with $b = 0.9$ (green cluster of points in Figure 6 at $M_{\rm lr} = M_{\rm targ}$), the targets typically lose about 10% of their pre-impact velocity. For $b = 0.7$ (red points), there is more significant slowing of the target. Our data does not provide a robust description of the dependence of the post-impact velocity on the impact parameter and impact velocity.

The projectile may be significantly deformed and disrupted during a hit-and-run event. The level of disruption of the projectile may be approximated by considering the reverse impact scenario: a fraction of the larger body impacts the smaller body. In this case, we estimate the interacting mass from the larger body with a simple geometric approximation. For the example geometry given in Figure 2, the cross-sectional area of the circular projectile interacting with the target is calculated. The apothem is given by $l - r$, and the central angle is $\phi = 2\cos^{-1}((l - r)/r)$. Then, the projectile collision cross section is

$$A_{\rm interact} = r^2(\pi - (\phi - \sin\phi)/2). \quad (46)$$

The interacting length through the target is approximated by the chord at $l/2$,

$$L_{\rm interact} = 2\sqrt{R^2 - (R - l/2)^2}. \quad (47)$$

And the interacting mass from the target is of order

$$M_{\rm interact} = A_{\rm interact} L_{\rm interact}. \quad (48)$$

Note that the interacting mass depends on the impact angle (through l).

To estimate the disruption of the projectile, we consider an idealized hit-and-run scenario between gravity-dominated bodies: the fraction of the target that does not intersect the projectile is sheared off with negligible change in momentum and gravitationally escapes the interacting mass. Hence, we ignore the escaping target mass and consider only the impact between $M_{\rm interact}$ and the projectile mass, $M_{\rm p}$.

The reverse impact is thus defined by $M_{\rm p}^{\dagger} = M_{\rm interact}$ and $M_{\rm targ}^{\dagger} = M_{\rm p}$, and the † denotes the reverse impact variables. For each impact angle, calculate $R_{C1}^{\dagger}$ for $M_{\rm tot}^{\dagger} = M_{\rm p}^{\dagger} + M_{\rm targ}^{\dagger}$, $Q_{{\rm RD},\gamma=1}^{\dagger *}$ from the principal disruption curve (Equation (28)), and $V_{\gamma=1}^{\dagger *}$ from Equation (30). The reverse variables are

$$\mu^{\dagger} = M_{\rm p}^{\dagger} M_{\rm targ}^{\dagger} / \left(M_{\rm p}^{\dagger} + M_{\rm targ}^{\dagger}\right), \quad (49)$$

$$\gamma^{\dagger} = M_{\rm p}^{\dagger} / M_{\rm targ}^{\dagger}. \quad (50)$$

The mass ratio correction from the principal disruption curve is

$$V^{\dagger *} = \left[\frac{1}{4}\frac{(\gamma^{\dagger} + 1)^2}{\gamma^{\dagger}}\right]^{1/(3\bar{\mu})} V_{\gamma=1}^{\dagger *}, \quad (51)$$

$$Q_{\rm RD}^{\dagger *} = Q_{{\rm RD},\gamma=1}^{\dagger *} \left(\frac{1}{4}\frac{(\gamma^{\dagger} + 1)^2}{\gamma^{\dagger}}\right)^{2/(3\bar{\mu})-1}. \quad (52)$$

Once the reverse impact disruption criteria is calculated, we use the universal law for the mass of the largest remnant to determine the collision regime for the projectile. If the projectile disrupts, then the size distribution of the projectile fragments may be estimated to first order from the disruption regime scaling laws.

5. TRANSITIONS BETWEEN COLLISION REGIMES

5.1. Empirical Transitions between Accretion, Erosion, and Hit-and-run

We have classified the collision outcome regime for all of our new simulations. The outcome is sensitive to the mass ratio of the two bodies, the impact parameter, and the impact velocity. Four regimes are mapped in Figure 10.

1. Accretion of some or all of the projectile onto the target ($M_{\rm lr} > M_{\rm targ}$ and $\xi > 1$, light blue squares).
2. Partial erosion of the target ($M_{\rm lr} < M_{\rm targ}$ and $\xi < 1$, dark blue squares).
3. Pure hit-and-run ($M_{\rm lr} = M_{\rm targ}$ and $\xi = 0$, green triangles).
4. Erosive hit-and-run ($M_{\rm lr}$ slightly less than $M_{\rm targ}$ and ξ slightly less than 0, red triangles).

Note that the 1:40 mass ratio simulations reach impact velocities that exceed the physics included in PKDGRAV; impact velocities greater than about 1 km s^{-1} should use a shock physics code. Hence, the transition to the erosive regime at high impact parameters could not be derived directly.

For impacts at small impact parameters (more head-on), the collision outcomes transition from accretion to erosion with increasing impact velocity. For more oblique impacts, the collision outcomes transition from merging to hit-and-run to erosion with increasing impact velocity. As suggested by Asphaug (2010), $b_{\rm crit}$ (red vertical line in Figure 10) is indeed a good indicator of the minimum impact parameter necessary to enter the hit-and-run regime. However, for $\gamma = 1$, we find a small region of erosive hit-and-run events when $b < b_{\rm crit}$. The use of $b_{\rm crit}$ to define grazing and non-grazing impacts makes the very simplifying assumption that the velocity vector of the center of mass of the projectile remains constant during the event. In reality, the projectile center of mass will be deflected to some extent during the encounter, and the true interactive mass will be larger than assumed here. The deflection is greatest for more equal-mass bodies, and a narrow region of erosive hit-and-run events is observed for $b = 0.35$ and $\gamma = 1$. Note that the transition between erosion and hit-and-run occurs near $b_{\rm crit}$ for all size bodies studied to date, from 1 km rubble-pile planetesimals (Leinhardt et al. 2000) to super-Earths (Marcus et al. 2009).

For grazing collisions, the hit-and-run regime is bounded by perfect merging at low impact velocities and the onset of disruption at high velocities. The projectile merges with the target when the impact velocity is less than the mutual escape

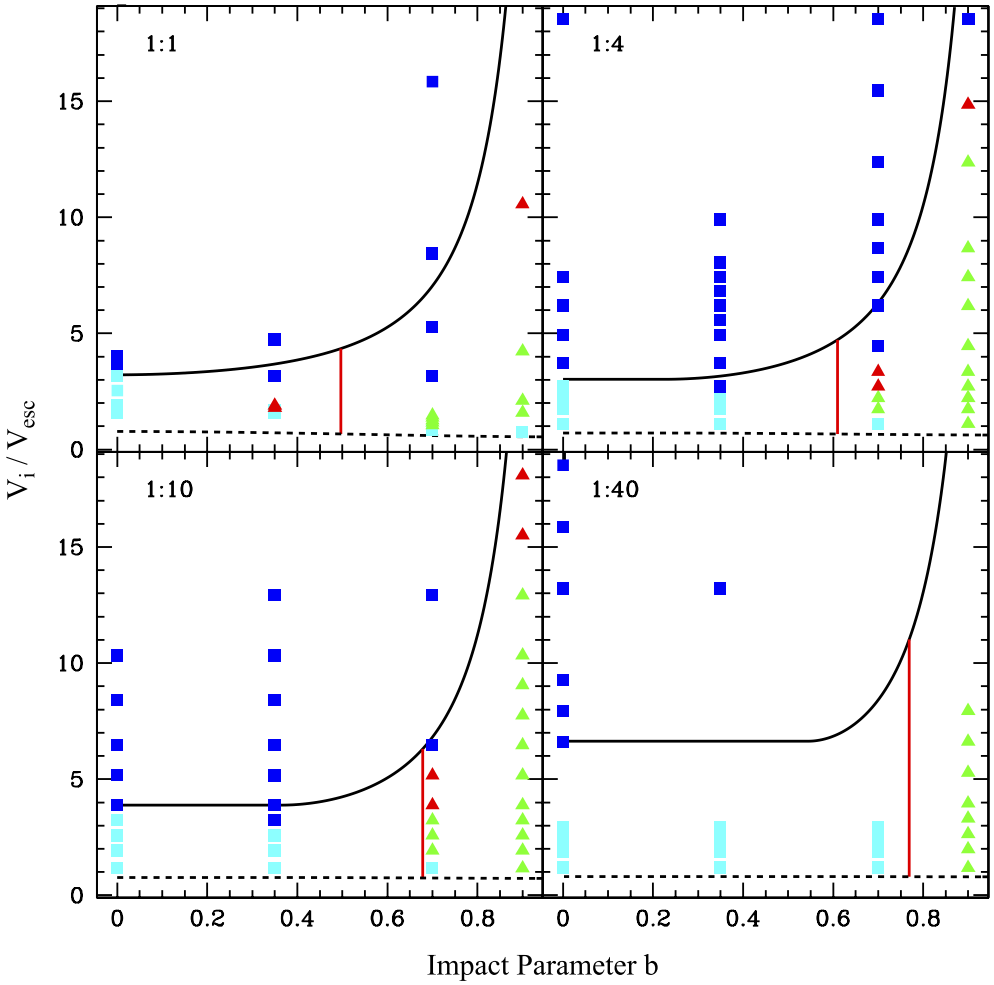

Figure 10. Map of the major collision regimes as a function of mass ratio, impact parameter, and impact velocity normalized by the escape velocity from the combined mass with radius R_{C1}. Cyan squares—a full or partial accretion event, $M_{\rm lr} > M_{\rm targ}$; blue squares—target is eroded, $M_{\rm lr} < M_{\rm targ}$; green triangles—ideal hit-and-run event, $M_{\rm lr} = M_{\rm targ}$; red triangles—erosive hit-and-run event, $M_{\rm lr}$ slightly less than $M_{\rm targ}$. Red vertical line corresponds to $b_{\rm crit}$ for the given mass ratio (Equation (6)). Black curve is onset of erosion predicted from the catastrophic disruption model (Section 3.1) with $c^* = 4.3$ and $\bar{\mu} = 0.35$; dashed black curve is predicted transition from perfect merging to hit-and-run (Equation (53)).

(A color version of this figure is available in the online journal.)

velocity (in other words, the velocity at infinity $V_{\rm inf}$ is zero). Since only a fraction of the projectile may interact in oblique impacts, the appropriate mutual escape velocity for perfect merging is slightly less than the mutual escape velocity from the total mass. Then the appropriate measure for merging is

$$V'_{\rm esc} = \sqrt{(2GM'/R')}, \quad (53)$$

where $M' = M_{\rm targ} + m_{\rm interact}$ and $R' = ((3M')/(4\pi\rho))^{1/3}$, assuming that the projectile and target have the same bulk density ρ. The boundary between merging and hit-and-run is well matched by Equation (53) in Figure 10 (dashed black line).

Of course, the concept of an interacting mass is a simplistic limit because it assumes that the part of the projectile that impacts the target can separate from the rest of the projectile without loss of momentum. In Figure 10, the only set of simulations that did not show a sharp transition from merging to hit-and-run is $\gamma = 0.1$ and $b = 0.7$. In this case, the impact parameter is very close to $b_{\rm crit} = 0.66$, and the outcomes include partial accretion of the projectile, erosive hit-and-run, and fully erosive collisions with increasing impact velocity.

Loss of momentum by the projectile in grazing collisions does lead to merging when $V_{\rm inf} > 0$; in Figure 9, note the nearly complete merging in the $\gamma = 1$ simulations for small values of $V_{\rm inf}$ with $b = 0.5$ and 0.9 (data from Agnor & Asphaug 2004a). For $V_{\rm inf}$ slightly above zero, merging occurs in graze-and-merge events (e.g., Leinhardt et al. 2010). In such cases, the two bodies hit, separate as nearly intact bodies with decreased velocity, and then merge upon a second collision. The impact velocity range for graze-and-merge outcomes is quite narrow; previous studies have demonstrated the small velocity increase needed to transition from perfect merging to graze-and-merge to hit-and-run (e.g., Canup 2004; Leinhardt et al. 2010). Concurrent with this work, the graze-and-merge regime has been explored in more detail using hydrodynamic SPH simulations by Genda et al. (2011b).

Grazing collisions transition out of hit-and-run to erosion of the target when the impact velocities reach the disruption regime. The transition to the disruption regime is a strong function of the impact parameter because of the rapidly shrinking projectile interaction mass and the dependence of the disruption criteria on the mass ratio and impact velocity.

Our general model for the catastrophic disruption criterion combined with the universal law for the mass of the largest remnant is used to derive the impact velocity needed to begin eroding the target mass ($M_{\rm lr} = M_{\rm targ}$, black line in Figure 10).

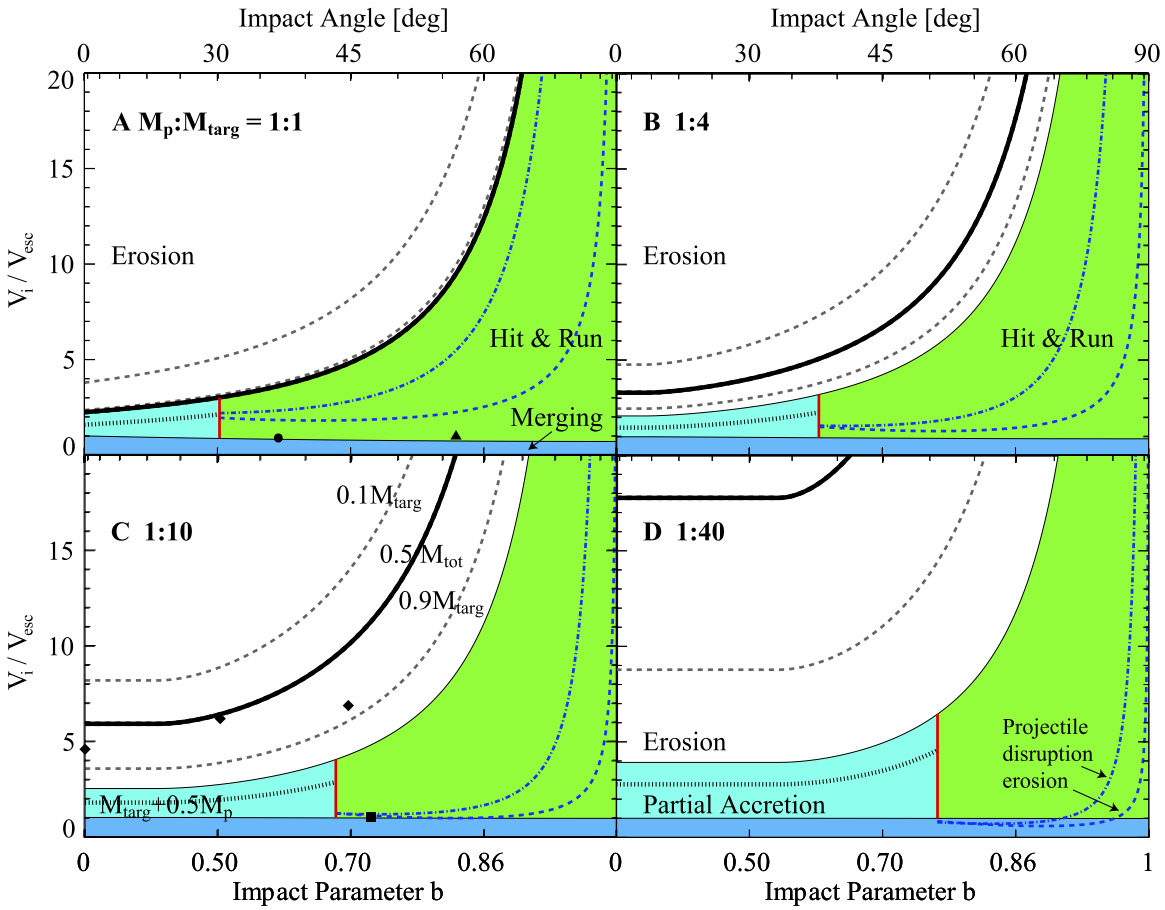

Figure 11. Predicted collision outcome maps using the analytic model for strengthless planets ($c^* = 1.9$ and $\bar{\mu} = 0.36$) for selected projectile-to-target mass ratios. Impact velocity is normalized by the mutual surface escape velocity assuming a bulk density of 3000 kg m^{-3}; impact parameter is spaced according to equal probability. Colored regions denote perfect merging (dark blue), partial accretion (light blue), net erosion to the target (white), and hit-and-run (green). The vertical red line denotes the onset of hit-and-run events at $b_{\rm crit}$. Thick black curve—critical disruption velocity for half the total mass remaining; gray dashed curves—10% and 90% of target mass in largest remnant; dotted curve—50% of projectile accreted; dot-dashed blue curve—catastrophic disruption of the projectile; dashed blue curve—erosion of the projectile. Example proposed giant impact events: (●) Haumea system (Leinhardt et al. 2010); (▲) Pluto-Charon (Canup 2005); (◆) Mercury (Benz et al. 2007); (■) Earth–Moon (Canup 2004).

(A color version of this figure is available in the online journal.)

Our new simulation data are best fit with a value of $c^* = 4.3$ and $\bar{\mu} = 0.35$. Our model for the disruption regime provides an excellent estimate for the transition to erosion of the target for the wide range of impact parameters considered here. In particular, the analytic model captures the sharp increase in the upper bound to the hit-and-run regime between $b = 0.7$ (45°) and 0.9 (64°).

5.2. Predicted Transitions between Accretion, Erosion, and Hit-and-run

Using our analytic model, we derive example collision outcome maps for collisions between protoplanets. We fit values of $\bar{\mu} = 0.36$ and $c^* = 1.9$ to the data from collisions between planet-sized bodies using SPH codes (Figure 4(B)). Collision maps, which are color-coded for outcome regime, are shown in Figure 11 for four mass ratios.

The details of the forward calculation of the collision regimes are given in the Appendix.[6] In Figure 11, the impact parameter axis is scaled by the probability of an impact at that angle. The probability of an impact within an interval $(\theta, \theta + d\theta)$ is proportional to $\sin(\theta)\cos(\theta)d\theta$ Shoemaker (1962). The corresponding impact angle is shown on the top axis with 5° tick intervals. The model assumes an abrupt transition between grazing and non-grazing impacts, which is certainly artificial. Near the critical impact parameter, collision outcomes will have elements from both the disruption and hit-and-run regimes.

Contours of impact velocities that correspond to a constant mass of the largest remnant are calculated using the general model for catastrophic disruption and the universal law or power law for the mass of the largest remnant (Equations (5) or (44)). In Figure 11, the thick black curve corresponds to the critical velocity for catastrophic disruption, where the largest remnant contains half the total mass. Note that this curve corresponds to the target erosion boundary for 1:1 scenarios (the transition from partial accretion (light blue) or hit-and-run (green) to erosion (white) regions). The gray dashed curves correspond to the impact velocity needed to disperse 10% and 90% of the target mass.

Between perfect merging and erosion of the target, there is a region of partial accretion of the projectile. For non-grazing impacts, the dotted curve corresponds to accretion of 50% of the projectile mass. Grazing impacts transition rapidly between perfect merging and hit-and-run with increasing impact velocity.

Most hit-and-run collisions with $M_{\rm p} \leqslant 0.1 M_{\rm targ}$ result in significant disruption of the projectile. In the collision outcome

[6] A code to generate collision outcome maps and to calculate specific impact scenarios is available from the authors.

maps, the onset of projectile erosion in a hit-and-run event is given by

$$V^{\dagger}_{i,\mathrm{lr=M^{\dagger}_{targ}}} = \sqrt{2Q_{R,\mathrm{lr=M^{\dagger}_{targ}}} M^{\dagger}_{\mathrm{tot}}/\mu^{\dagger}}. \quad (54)$$

Note that for impact parameters near b_{crit}, $M^{\dagger}_{\mathrm{p}} \sim M^{\dagger}_{\mathrm{targ}}$ for projectile-to-target mass ratios less than about 0.1. Thus the velocity contours of constant remnant mass intersect for catastrophic disruption ($M^{\dagger}_{\mathrm{lr}} = 0.5M^{\dagger}_{\mathrm{tot}}$) and onset of projectile erosion ($M^{\dagger}_{\mathrm{lr}} = M^{\dagger}_{\mathrm{targ}}$). Furthermore, there is a minima in the projectile erosion curve at an optimal fraction of total interacting mass from the target (in other words, the reverse projectile-to-target mass ratio is varying with impact parameter). The two velocity contours diverge at higher impact parameter as $M^{\dagger}_{\mathrm{p}}$ becomes much less than $M^{\dagger}_{\mathrm{targ}}$.

Collision maps for planetesimals are presented in Section 6.2.1, and the implications of the diversity of collision outcomes for planet formation are discussed in Section 6.3.

6. DISCUSSION

6.1. Scaling of Collision Outcomes in the Gravity Regime

For all gravity-regime bodies studied to date, collision outcomes are strikingly similar for a tremendous range of target composition and size. Furthermore, the transitions between the major collision regimes (merging, hit-and-run, disruption, and super-catastrophic disruption) occur under similarly scaled conditions. The types of bodies studied, ranging from km to several 1000's km in size, included rubble-pile and porous planetesimals (this work, Stewart & Leinhardt 2009; Benz 2000; Jutzi et al. 2010; Korycansky & Asphaug 2009), pure rock or pure ice planetesimals with strength (Benz & Asphaug 1999; Leinhardt & Stewart 2009; Jutzi et al. 2010), strengthless differentiated rock and iron planets (Benz et al. 1988, 2007; Agnor & Asphaug 2004a; Marcus et al. 2009; Genda et al. 2011b), strengthless differentiated water and rock planets (Marcus et al. 2010b), and strengthless pure rock planets (Marcus et al. 2009). The studies focused on a variety of stages during planet formation, from accretion of planetesimals to destruction of planets; thus, the impact velocities ranged from $\sim$1 m s^{-1} to over 100 km s^{-1}. The computational methods included three different shock physics codes and two N-body codes. Our analysis of the results from these studies suggests that the same scaling laws may be applied over an incredibly broad range of impact scenarios during planet formation.

As stressed by Asphaug (2010), similarity of outcome is not the same as true scale invariance. He notes that scale invariance applies only for idealized incompressible, self-gravitating inviscid fluid planets. In reality, many aspects of collision outcomes will not scale simply with size, e.g., the mass of collision-produced melt depends on the specifics of impact velocity, target composition, and the internal temperature and pressure history. Here, we investigated the similarity of the dynamics of collision outcomes for a variety of non-ideal gravity-regime bodies, from icy planetesimals to differentiated super-Earths. Specifically, we developed scaling laws to define the mass and velocity distributions of bodies after any gravity-regime collision.

Why do the dynamics of collision outcomes appear to scale similarly with size in the gravity regime? At impact velocities just above the escape velocity, momentum dominates the outcome at all scales. Hence, the transition from merging to hit-and-run depends primarily on the geometric cross section of the collision for all size bodies. As impact velocities increase, the energy required for disruption is dominated by the gravitational dispersal of fragments rather than the energy required to shatter an intact body into small pieces (Melosh & Ryan 1997). As a result, erosive outcomes require that the velocity of the fragments exceed a critical value that relies primarily upon the gravitational potential of the total colliding mass.

For small bodies, the critical fragment velocity may be reached with impact velocities that impart negligible irreversible work on the materials (Figure 4). For larger bodies, the critical velocity requires sufficiently high impact velocities that strong shock waves are formed. The shock wave permanently deforms the materials and, in the process, reduces the total energy available for the final velocity distribution of fragments. The energy of deformation is often referred to as "waste heat"; for a fixed impact energy, a larger fraction of waste heat is generated with increasing impact velocity (primarily due to the onset of shock-induced melting and vaporization at high shock pressures). As a result, the catastrophic disruption criteria increases with increasing impact velocity (Equation (3)).

Based on currently available data we argue that in the disruption regime the dynamics of the outcome is similar over the entire gravity regime when scaled by the catastrophic disruption criteria. The post-collision size distribution is similar, as it is controlled by the largest remnant and the gravitationally accreted clumps from the shattered parent bodies. The general catastrophic disruption law accounts for both the increasing gravitational potential with total mass of the colliding bodies and the increase in waste heat at higher impact velocities (Housen & Holsapple 1990).

The development of Equation (3) relied upon the concept of a coupling parameter, $\Lambda \propto R_{\mathrm{p}} V_i^{\bar{\mu}}$, a point source approximation of the coupling of the projectile's energy and momentum into the target (see Holsapple & Schmidt 1987). The velocity exponent $\bar{\mu}$ is bounded by pure momentum coupling ($\bar{\mu} = 1/3$) and pure energy coupling ($\bar{\mu} = 2/3$). In the gravity regime, the coupling parameter distills the physical response of the geologic material into the variable $\bar{\mu}$. Some constraints on $\bar{\mu}$ are available from laboratory cratering experiments: e.g., $\bar{\mu} = 0.4$ for sand and $\bar{\mu} = 0.55$ for water (Holsapple & Schmidt 1987). Here, we fit the coupling parameter to the numerical simulation results for disruption of a wide variety of materials. The derived best-fit range of $0.33 \leqslant \bar{\mu} \leqslant 0.37$ is close to pure momentum scaling.

Why does the concept of a point source approximation apply to collisions between comparably sized planetary bodies? The point source approximation was developed for impact cratering by a finite-size projectile onto a half-space target. Holsapple & Schmidt (1987) show that the concept of a point source is equivalent to a variety of models that describe a similar material velocity field far from the impact point. In the case of catastrophic disruption, the late-time far-field criteria is a fragment size–velocity distributions where half the mass is escaping the gravitational potential of the largest remnant. The principal dynamical factors governing the collision are incorporated into the Q'^{*}_{RD} formulation: relative velocity, mass ratio, impact parameter, and bulk density. The similar outcomes of collisions with similar Q_R/Q'^{*}_{RD} indicate that the remaining details of how the energy and momentum are distributed into the target and projectile during the initial stage of the collision are negligible in determining the late time dynamics following a catastrophic disruption event.

In summary, the primary factors that bound the different collision outcome regimes scale similarly with size in the gravity regime: momentum, geometric cross section, and normalized critical impact energy ($Q'^{*}_{\rm RD}$). Other factors that lead to second-order perturbations to the dynamics of the collision outcomes are discussed in the next section.

6.2. Scaling Laws' Limits of Applicability

Planet formation involves a vast range of bodies with distinct physical characteristics, including dust aggregates, rubble-pile planetesimals, differentiated molten and solid protoplanets, solid planets with extended atmospheres, and gas-dominated planets. The constituent materials (iron-alloys, silicates, ices, and gases) span orders of magnitude in density and material strength. The complex and time-varying physical properties of planetary bodies significantly limit the application of any single equation to all bodies over the course of planet formation. And yet, judicious simplification is necessary for planet formation simulations to be both physically robust and computationally tractable.

We have focused on developing scaling laws that describe the dynamical outcome of collisions between any two gravity-dominated bodies. The dynamical outcome from collisions seems to be rather insensitive to the internal composition, when the results are scaled by the appropriate value for $Q^{*}_{\rm RD}$. However, the types of bodies studied to date do not contain any gas mass fraction (see, for example, Kobayashi et al. 2011), and so the scaling laws may need modification for a planet with a significantly different internal structure than the differentiated and homogeneous planets included in this study. One area that warrants further investigation is the sensitivity of the velocity of the largest remnant to the internal structure/composition (Figure 6).

The role of tidal effects during collisions or in close encounters may be important factors during the fragmentation of planetary bodies (Asphaug et al. 2006; Asphaug 2010). In this work, all bodies are assumed to be approximately spherical at the time of impact. Tidal affects will change the interacting mass and contribute to the fragmentation process in ways that lead to different size and velocity distributions than found here.

Similarly, the role of pre-impact spin during collisions has received modest attention (Leinhardt et al. 2000; Canup 2008). While the net spin of a growing body may essentially average near zero during the rapid growth phase where collisions are frequent, the effect of pre-impact spin and the collision angular momentum may be very important in the final giant impact phase of planet formation (Agnor et al. 1999). While we did not consider any pre-impact spin in this study, a few simulations with high collision angular momentum are notable. In 1:1 collisions with $0 < b < b_{\rm crit}$ (Table 1 in this work and Table 1 in Leinhardt et al. 2000), the catastrophic disruption criterion is less than the value at $b = 0$ (e.g., closed and open stars in Figure 4). We interpret the lower disruption criterion with pre-impact spin to arise from the significant collision angular momentum. As a result, the gravitational potential is reduced and dispersal requires slightly less energy. We suggest that future work investigate the possibility of using the reduction in the gravitational potential due to pre-impact and collision angular momentum to account for the first-order affects of spin. Specifically, the spin-modified catastrophic disruption criterion may remain at a constant offset (c^{*}) from the spin-modified gravitational potential.

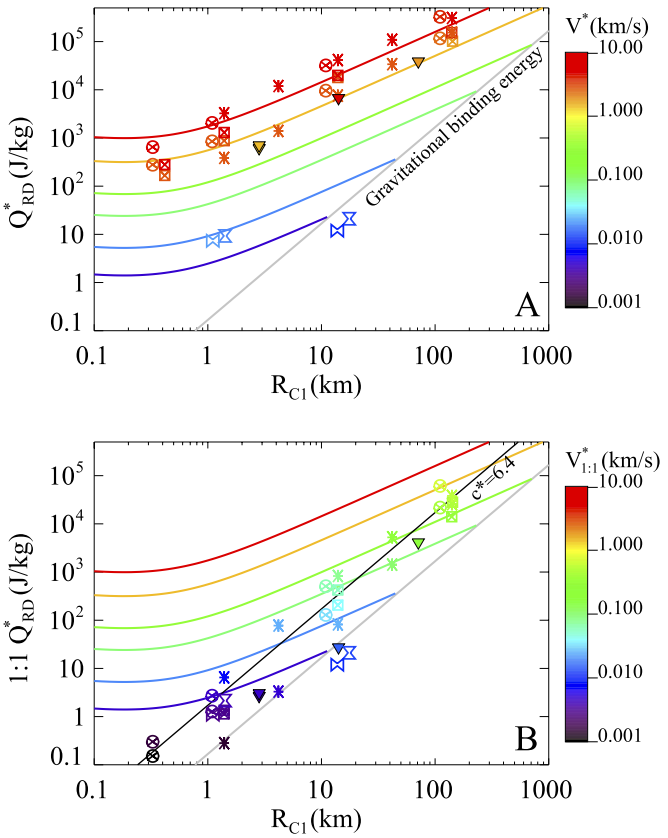

Figure 12. Catastrophic disruption simulation results for strong rock targets (porous and nonporous). Same notation as in Figure 4 and Table 3. (A) Simulation data corrected to an equivalent head-on impact. (B) Simulation data converted to an equivalent equal-mass disruption criteria. The results for critical velocities from m s^{-1} to 5 km s^{-1} demonstrate that energy scaling is incorrect. Best-fit $Q^{*}_{\rm RD}$ curves with $\bar{\mu} = 0.35$ and $c^{*} = 6.4$ for $V^{*} = 0.005$, 0.02, 0.1, 0.3, 1.5, and 5 km s^{-1}.

(A color version of this figure is available in the online journal.)

6.2.1. Strength and Porosity in the Gravity Regime

The study of catastrophic disruption of strong rock targets has been motivated by collisional evolution studies of the asteroid and Kuiper belts. The strength models were tested by fitting laboratory quasi-static strength measurements and fragment size distributions from head-on disruption experiments. Particular attention was paid to the development of the model for tensile fracture (Benz & Asphaug 1994), as the tensile strength dominates the catastrophic disruption criterion for head-on impacts in the strength regime.

Results from several numerical simulations of catastrophic disruption of strong rock targets in the gravity regime are shown in Figure 12. The head-on basalt disruption data at impact velocities of 3 and 5 km s^{-1} ($*$) are shown from the canonical study by Benz & Asphaug (1999) using the SPH code with the detailed tensile strength model. Using the same code, Benz (2000) studied the disruption of strong nonporous basalt (hourglass) and a macroporous target, composed of overlapping clusters of SPH particles representing strong interconnected boulders ($\bowtie$), at very low impact velocities (5–40 m s^{-1}) and $b = 0.7$. In Figure 12, the 10 km target data, which fall below the specific gravitational binding energy, are derived from the equal-mass collisions presented in Benz's Figure 5 and will be discussed below. The Benz (2000) 1 km data are less certain using our catastrophic disruption variables because both impact

velocity and mass ratio were varied and the specific values were not reported. Nevertheless, the significant offset in the disruption criteria is irrefutable evidence that pure energy scaling does not apply. In fact, the total dispersion in the specific impact energy is slightly larger than can be accommodated by the momentum scaling limit of $\bar{\mu} = 1/3$, which is likely a result of differences in the details of the strength models.

More recent simulations (⊗, ⊠) by Jutzi et al. (2010) with critical velocities of 3 and 5 km s^{-1} fall in-between the data from Benz & Asphaug (1999). Their work uses the same SPH code with an updated strength model that includes the extra dissipation of microporosity. Simulations using the shock physics code, CTH, with different shear and tensile strength models yield similar results as found for nonporous basalt targets using the SPH code (▼; Leinhardt & Stewart 2009).

In Figure 12, the strong target data, with mass ratios from 1:1 to almost 1:45,000 and impact velocities from 0.001 to 5 km s^{-1}, are best fit by $\bar{\mu} = 0.35$ and $c^* = 6.4$. The equivalent equal-mass disruption data have c^* values from 1 to 20. For comparison, the best fit to only the PKDGRAV rubble-pile data is $c^* = 5.5$ and $\bar{\mu} = 0.365$. We note that the data from Jutzi et al. (2010) and the 1 km targets from Benz (2000) nicely cluster around the best-fit principal disruption curve. Jutzi et al. (2010) fit their 3 and 5 km s^{-1} data with $\bar{\mu} = 0.43$; however, such a high value for $\bar{\mu}$ cannot simultaneously fit the data at lower velocities. The two-dimensional simulations from Leinhardt & Stewart (2009) fall systematically below the best-fit curve. The 3 and 5 km s^{-1} head-on data from Benz & Asphaug (1999) have a dispersion greater than can be explained with our model; the low- and high-velocity data fall below and above the best-fit curve, respectively. The data from Benz & Asphaug (1999) and the 10 km data from Benz (2000) were excluded from the global fits presented in Section 3.1.3.

The 10 km equal-mass data from Benz (2000) (⋈ and hourglass) require closer examination. At an impact angle of 45 deg, all 1:1 data on weaker bodies pass through the hit-and-run regime. However, both the nonporous and porous data show disruption results similar to the non-grazing regime. We interpret the non-grazing outcome to be due to the high shear strength of the target preventing a hit-and-run outcome. We hypothesize that the disruptive outcome and disruption energy below the gravitational binding energy are related to the strength and angular momentum of the event. A collision between two equal-size strong bodies has a larger interacting mass than assumed in our model, so the adjustment from the oblique to equivalent head-on collision disruption energy is overestimated. In addition, the collision generates significant spin angular momentum. The angular momentum reduces the effective gravitational binding energy and, similarly, the required disruption energy. These data illustrate the need to better understand the physical properties of strong targets in oblique impacts and the role of angular momentum.

In the strong rock target simulations, the typical limiting shear strength is 3.5 GPa, comparable to the quasi-static shear strength in laboratory rock under high confining pressure. In the SPH simulations, the shear strength was fixed throughout the simulation. In the CTH simulations, the shear strength was dependent on the confining pressure and the accumulation of damage (e.g., fractures). Leinhardt & Stewart (2009) demonstrated that shear strength is important for the size bodies considered here, which are usually considered to be purely in the gravity regime. Higher shear strength leads to greater dissipation of the shock energy into material deformation; hence, higher specific energies are required to disrupt stronger targets. None of the published work has investigated the role of strain rate on zones of shear localization in catastrophic disruption simulations, which leads to significant reduction of shear strength during impact cratering events (e.g., Senft & Stewart 2009). More work is needed to develop more sophisticated shear strength models for strong rock targets and to validate model calculations for oblique impacts.

There has been some recent work on the catastrophic disruption of porous planetesimals. Porosity has been modeled in three different ways: as hard sphere rubble piles with various bulk densities in studies using PKDGRAV (see references in Figure 4), macroporous overlapping clusters of SPH particles representing intact boulders (Benz 2000), and microporous bodies using a constitutive model for porosity in an SPH code (Jutzi et al. 2010). The SPH simulations found significant effects of porosity in the strength regime; however, porosity was a second-order effect in the gravity regime, and the catastrophic disruption criterion agreed with the nonporous simulations when the data were normalized by the difference in bulk density (Jutzi et al. 2010). The low-velocity macroporous SPH simulation results in the gravity regime overlap with the PKDGRAV rubble-pile results. Finally, Jutzi et al. (2010) found similar fragment size and velocity distributions between their porous and nonporous gravity regime results.

We note that the transition between the gravity and the strength regime should be handled carefully and appropriate coefficients should be chosen for different material composition and strength. There appears to be significantly more variation in the disruption criterion in the strength regime compared to the gravity regime; however, future work should consider whether or not a scaling analysis similar to the one presented here may capture most of the variance.

6.2.2. Other Collision Outcomes

In cases where the impact velocity is above the escape velocity but the mass of the projectile is too small to lead to disruption, some material will escape the target in the form of crater ejecta. In recent work, Housen & Holsapple (2011) has conducted a detailed study of the scaling of ejecta from impact craters. Based on many laboratory experiments, Housen & Holsapple (2011) find that approximately $0.01 M_{\rm p}$ of material achieves escape velocity in cratering events at $V_i \sim V_{\rm esc}$ (see their Figure 16). Empirical fits to the material eroded during cratering events onto self-gravitating bodies have also been studied numerically by Svetov (2011).

The bulk composition of a body may change during planet formation by either preferentially accreting material of a certain composition (e.g., ice fragments chipped off smaller bodies) or by stripping of mantle material. The loss of a mantle during catastrophic disruption has been studied for rock/iron and water/rock differentiated planets by Marcus et al. (2009, 2010b). They developed two models to calculate the resulting change in the mantle mass fraction that bound the simulation results. Their method for calculating the change in composition is described in the Appendix and may be incorporated into planet formation studies that track the composition of growing and eroding planets (Stewart & Leinhardt 2011).

Previous work has addressed collision outcomes in the strength regime to various levels of generality. We refer the reader to Beauge & Aarseth (1990) and Kenyon & Bromley (2008), and references therein.

6.3. Implications for Planet Formation

6.3.1. Giant Impact Events

Even with limited understanding of the full dynamics of collision outcomes, the significant role of giant impact events in determining the final physical properties of rocky/icy planets has been recognized (e.g., Agnor et al. 1999; Ida & Lin 2010). Any event between similar-sized bodies ($\gamma \gtrsim 0.1$) may be considered a giant impact event, although the outcomes are more dramatic for larger mass bodies (Asphaug et al. 2006; Asphaug 2010).

Agnor et al. (1999) found that the most common collision events at the end stage of terrestrial planet formation (under our solar system conditions) have $\gamma \sim 0.01$–0.2 and V_i from about 1 to $4V_{\rm esc}$. Over this range of mass ratios and impact velocities, collision outcomes span all the regimes: accretion, erosion, and hit-and-run. In Figure 11(C), note that $b_{\rm crit} = 0.66$ for $\gamma = 0.1$; hence, about half of all impacts fall in the regime that transitions from accretion to erosion and half transition through a hit-and-run regime. Hence, the implementation of self-consistent scaling laws to describe collision outcomes is crucial to the accurate treatment of the giant impact phase of planet formation. Although Agnor et al. (1999) typically found that impact velocities fell in the range of 1 to $2V_{\rm esc}$, temporary dynamical excitation by migrating giant planets may further increase the impact velocities in our solar system and in exoplanetary systems (Nagasawa et al. 2005; Morbidelli 2010; Walsh et al. 2011). Therefore, robust characterization of all collision outcomes is necessary for any planet formation calculation.

With the strong dependence of collision outcome on the mass ratio, the final stage of planet formation is likely to produce more diverse outcomes than previously anticipated. As argued by Asphaug (2010), the increased frequency of hit-and-run events during the giant impact stage may routinely lead to compositional modification of the second-largest body. As shown in Figure 11, the escaping projectile is nearly always eroded in hit-and-run events. Consequently, the atmosphere, hydrosphere, and even the mantle of these bodies may be stripped away. Such interesting details may now be explored directly in planet formation simulations. Asphaug (2010) suggested that the growth of large rocky planets occurs often by a series of hit-and-run events followed by an eventual merger. Under these circumstances, each accreting protoplanet could have been partly devolatilized before merging. In this manner, the final composition of planets may be altered significantly compared to the initial protoplanets during accretion into the final planets.

Note that our analytic calculation of collision outcomes agrees very well with the proposed giant impact scenarios for the formation of the Haumea system (Leinhardt et al. 2010), the formation of Pluto and Charon (Canup 2005), the formation of Earth's moon (Canup 2004), and the increased density of Mercury (Benz et al. 2007) (Figure 11). The formation models plotted for Haumea and Pluto-Charon are the result of graze-and-merge events, where two equal-mass bodies collide and separate nearly intact. The loss of velocity by the first collision leads to a merging upon a second collision, creating a final body with enough angular momentum to spin off a disk of material. In contrast, the canonical formation of the Moon involves a collision where the projectile is disrupted upon the first impact. The analytic calculation for disruption of the projectile agrees very well with these moon-forming studies. Because the giant impact phase of planet formation is dominated by collisions slightly above the mutual escape velocity, the probability scaled axis in Figure 11 emphasizes the high likelihood that the giant impacts will be on the boundary of the merging and hit-and-run regimes (see also Stewart & Leinhardt 2011).

Given the range of impact velocities found by Agnor et al. (1999) in the giant impact stage (up to about $6V_{\rm esc}$), stripping the mantle from Mercury by a catastrophic disruption event is reasonably probable. Recently, collision outcomes alone have been used to define a limit to the possible density of super-Earth mass exoplanets (1–10 $M_{\otimes}$). Based on the criterion to strip off mantle material during catastrophic disruption, Marcus et al. (2010a) used the extremely high impact velocities required to disrupt 1–10 Earth-mass planets to place an empirical limit to the iron fraction of a planet that has suffered a single catastrophic impact event. The prediction is in very good agreement with observations of rocky exoplanets (e.g., Kepler 10b and 55 Cnc e; Winn et al. 2011; Batalha et al. 2011). Consideration should be given to the potential for stripping mantles off the planets by erosive hit-and-run events, e.g., the smaller projectile has its mantle stripped but it is never incorporated into a larger body.

6.3.2. Collisional Evolution of Small Body Populations

The asteroid and Kuiper belts contain a valuable record of the dynamics of the solar system. The collisional evolution and dynamical clearing of these reservoirs of small bodies has been modeled extensively (e.g. Nesvorný et al. 2002; Bottke et al. 2002; Morbidelli et al. 2008; Kenyon et al. 2008). Observations of asteroid families, in particular, have been important in the study of planetary dynamics and impact processes. Asteroid families and their associated dust bands are believed to have formed in recent catastrophic impact events (Nesvorný et al. 2003). Simulations of asteroid disruption have been compared to observations of the size and velocity distributions of asteroid families to derive possible impact scenarios. For example, Nesvorný et al. (2006) simulated the formation and dynamical evolution of the Karin family. Using the same SPH code and strength model used by Benz & Asphaug (1999), their best-fit scenarios for the Karin family involve a 5–7 km s^{-1} impact onto a 15 km target with a mass ratio of 1:200 and $M_{\rm lr} \sim 0.1$–$0.2 M_{\rm targ}$ (Figure 13). In order to match this combination of impact energy and largest remnant mass with our analytic model, a value of c^* of approximately 20 is required, which is significantly higher than the best-fit value of 6.4 derived here for strong targets. Figure 13 presents collision outcome maps for the best fit for all small bodies ($c^* = 5$) and the very strong bodies inferred from the asteroid-family formation simulations ($c^* = 20$). Catastrophic disruption begins at impact velocities of $107V_{\rm esc}$ for the generic small body, whereas values about twice as high are required for the strong targets simulated by Nesvorný et al. (2006).

In addition to studying individual collisions, the collisional evolution of the asteroid belt size distribution has been studied in detail (e.g., Davis et al. 1979; Bottke et al. 2005; Morbidelli et al. 2009). Such studies seek to understand the relative weight of collisional versus dynamical clearing of the belt and the initial size distribution of planetesimals. From our discussion of the role of strength during the evolution of planetesimals from weak aggregates to protoplanets, it is clear that a single catastrophic disruption criterion cannot apply at all times.

Also, the influence of mass ratio on the disruption criterion will be important if the first planetesimals were born big. Morbidelli et al. (2009) argue that the observed size–frequency distribution of asteroids is best fit by an initial population of

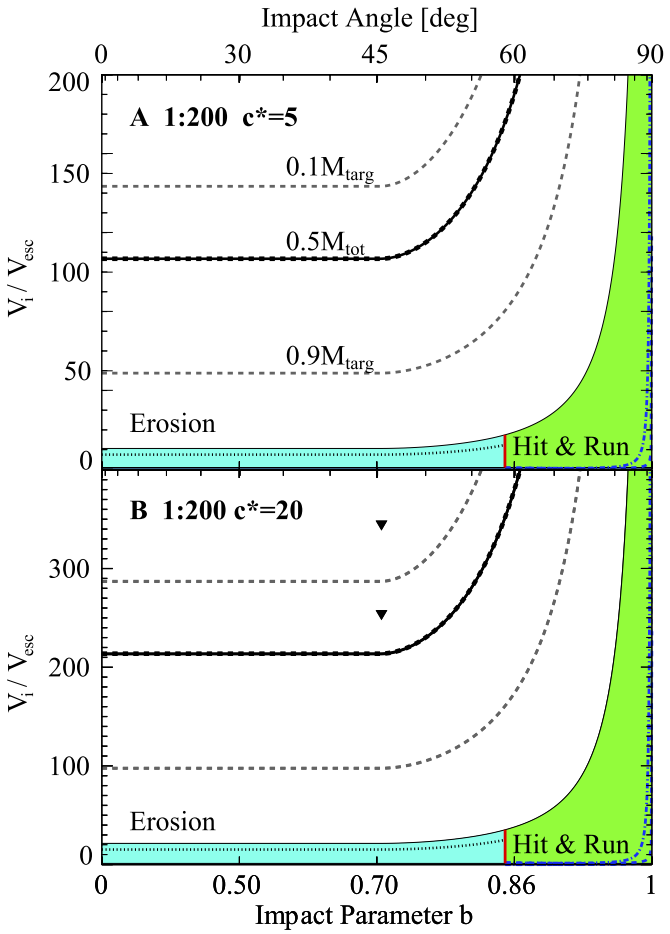

Figure 13. Predicted collision outcome maps for small projectiles ($M_p : M_{targ} = 1 : 200$) using the analytic model for (A) a nominal planetesimal with $c^* = 5$ and (B) best fit to asteroid family formation simulations with $c^* = 20$. Axes, colors, and line notations are the same as defined in Figure 11. Proposed asteroid family-forming events with $M_{lr} \sim 0.1$–$0.2 M_{targ}$: (▼) Karin (Nesvorný et al. 2006).

(A color version of this figure is available in the online journal.)

planetesimals that were hundreds of km in size. (Note this suggestion has not been fully accepted as a requirement for the observed size distribution of asteroids; see Weidenschilling 2011.) Two processes have been proposed to form km to 100 km scale initial planetesimals: turbulent concentration (Cuzzi et al. 2008) and streaming instabilities (Johansen et al. 2007). A mechanism to form km scale planetesimals is attractive because it could help bypass the so-called meter size barrier, the size particle that radially drifts in toward the Sun faster than it can grow. In the collision evolution model by Morbidelli et al. (2009), the catastrophic disruption threshold is the angle-averaged 5 km s^{-1} constant velocity curve for strong basalt from Benz & Asphaug (1999). Note, however, that the proposed mechanisms to form km scale planetesimals would generate weak aggregates of small (e.g., cm to m size) particles. These aggregates will be comparable to simulations of weaker materials. Morbidelli et al. (2009) considered a collisional evolution simulation using a catastrophic disruption criteria that was a factor of eight lower than the basalt criteria. They note that the size–frequency distribution was not significantly affected by the larger amount of collisional grinding in the one test case; however, they could not form the lunar to Mars-size embryos expected in the early asteroid belt. They reject the lower disruption criteria as being inconsistent with observations (and their initial assumed population of 1 km radius bodies).

Here, we stress that a population of comparably sized bodies will be subject to the lowest possible disruption criteria, $Q^*_{RD,\gamma=1}$. For example, two colliding bodies with individual radii of 1 km and density of rock have $R_{C1} \sim 2$ km. Using Equation (30) with $c^* = 5$ and $\bar{\mu} = 0.37$ for small bodies, $Q^*_{RD,\gamma=1} = 5.3$ J kg^{-1} and the corresponding $V^*_{\gamma=1}$ is 6.5 m s^{-1}. For a 45 deg impact, the value for Q'^*_{RD} rises by almost a factor of five (Equation (23)) and $V^* = 14$ m s^{-1}. Note that this value of Q'^*_{RD} is more than a factor of 100 lower than the 5 km s^{-1} strong basalt disruption curve (Figure 12). This example illustrates the need to incorporate self-consistent disruption criteria that account for impact velocity and mass ratio in order to infer the magnitude of collisional evolution in a given population of bodies.

6.3.3. Application of Collision Scaling Laws in Planet Formation

To date, all numerical implementations of fragmentation during collisional growth of planets assume pure energy scaling. That is, $\bar{\mu}$ is assumed to be 2/3 and, thus, there is no velocity dependence in the catastrophic disruption criterion (Equation (3)). In contrast, the vast collection of data in the gravity regime indicates that catastrophic disruption is best fit by nearly pure momentum scaling. With nearly linear dependence on the critical velocity, the criterion for fragmentation may vary by orders of magnitude during planet formation (Stewart & Leinhardt 2009). Several studies have investigated shifting a single reference size-dependent disruption curve by a constant value that is fixed over the course of the simulation to represent stronger or weaker bodies, but none have considered a fragmentation criterion that may be variable in time and space.

Furthermore, planet formation models have not included the dependence on the mass ratio of the bodies on the disruption criterion. A recent simple treatment of the collision parameters required for hit-and-run versus merging indicated that planet formation was only slightly delayed compared to simulations with only merging outcomes (Kokubo & Genda 2010). However, this work did not include any treatment of fragmentation. Based on our calculation of the region of partial accretion for non-grazing impacts and projectile disruption in hit-and-run events (Figure 11), fragmentation is a critical component of the end stage of planet formation. Numerical simulations cannot assume pure merging or pure hit-and-run. The diversity of collision outcomes during the end stage of planet formation is described in detail in the companion paper, which uses the impact parameters from recent *N*-body simulations that assumed perfect merging to calculate the range of collision outcomes predicted by our model (Stewart & Leinhardt 2011).

In this work, the general catastrophic disruption law relies upon only two independent material constants ($\bar{\mu}$ and c^*; q_g is related through Equation (29)) and the impact conditions (mass, mass ratio, impact angle, and velocity). The material parameters are well constrained. The coupling parameter $\bar{\mu}$ is tightly constrained by a large data set (Figure 4) to fall close to pure momentum scaling (0.33–0.37).

The energy dissipation parameter c^* is a measure of the physical characteristics of the body. For small bodies with varying composition and strength, we find $c^* = 5 \pm 2$. As bodies grow into protoplanets (~1000 km), they heat internally from the heat of accretion and radioactive decay. Then, the energy dissipation parameter for hydrodynamic planets and planetesimals, $c^* = 1.9 \pm 0.3$, is appropriate. After

molten planetesimals recrystallize, they will be temporarily stronger until they experience sub-catastrophic shattering impact events. Based on the strong rock simulations, collisional evolution models should test for sensitivity to values of c^* up to about 20.

Two additional parameters describe the distribution of fragments during erosive collisions. β is the exponent to the size distribution of small fragments and η is the slope of the power-law size distribution for the largest fragment in the super-catastrophic regime. The values for β and η are also tightly constrained by simulations and laboratory experiments, respectively, and may be considered, to first order, constant.

7. CONCLUSIONS

We present a completely self-consistent set of scaling laws to describe the dynamical outcome of a collision between any two bodies in the gravity regime. The scaling laws rely upon the concept of the interacting mass, the fraction of the projectile involved in the collision. Using the interacting mass, we derive a general catastrophic disruption scaling law. The general forms include two independent material parameters: the coupling parameter $\bar{\mu}$ and the energy dissipation parameter c^*. The catastrophic disruption criterion is used to bound the transitions between collision outcome regimes. The subsequent description for the size and velocity of collision fragments is derived in closed-form analytic equations with two well-constrained parameters.

With this powerful new tool to describe the dynamical outcome of collisions, the physics of collisions in planet formation models will have much greater fidelity. Planet formation models now have a very small number of free parameters to describe collision outcomes (primarily the energy dissipation parameter, c^*). With a more robust physical model for collisions, more detailed factors may be studied, such as the evolution of composition during planet formation. Alternatively, other fundamental aspects of planet formation may be investigated more deeply (e.g., migration) now that the collision model is tightly constrained.

Future work should now bring greater scrutiny to the scaling laws used in the strength regime. Although this regime has historically been better constrained by the abundance of laboratory experiments, self-consistent scaling laws also require attention to the dependence of fragmentation on the impact velocity, mass ratio, and impact angle.

By fully constraining the dynamics of collisions in the gravity regime, this work represents a major advancement in the robustness of simulations of planet formation and the collisional evolution of populations of planets.

The N-body calculations were run using the University of Cambridge, Astrophysical Fluids Research Group computational facilities. Z.M.L. is supported by an Advanced STFC fellowship; S.T.S. by NASA grant NNX09AP27G.

APPENDIX

DESCRIPTION OF VARIABLES AND SUMMARY OF COLLISION MODEL

A description of variables and annotations is given in Table 2. The compilation of simulation data on catastrophic disruption presented in Figures 4 and 12 is summarized in Table 3. A summary of all the PKDGRAV simulations conducted in this study is presented in Table 4.

Table 2
Summary of Primary Variables and Annotations

Symbol	Definition
Material parameters	
c^*	Head-on equal-mass disruption energy in units of specific gravitational binding energy
$\bar{\mu}$	Velocity exponent in coupling parameter
β	Slope of fragment size distribution
η	Exponent in power-law fragment distribution in super-catastrophic regime
Principal variables	
V, V_i	Impact velocity
$V_{\rm esc}$, $V_{\rm inf}$	Escape velocity, velocity at infinity
Q	Specific impact energy
Q_R	Specific impact energy for the collision in center of mass frame
$Q^*_{\rm RD}$	Catastrophic disruption criteria—specific impact energy to disperse half the total mass
M, m	Mass
R_{C1}	Radius of total mass in a body with density 1000 kg m^{-3}
μ	Reduced mass
γ	Projectile-to-target mass ratio
α	Mass fraction of the projectile that intersects the target
q_g	Coefficient of gravity term in general formula for Q^*_{RD}
ξ	Accretion efficiency
v	Velocity of fragments
ρ	Density
Geometric variables	
θ	Impact angle (0 is head-on)
b	Impact parameter sin(θ)
$b_{\rm crit}$	Critical impact parameter denoting transition from non-grazing to grazing collision
R	Target radius
r	Projectile radius
D	Diameter
$l/(2r)$	Fraction of projectile diameter that overlaps with target
Superscripts	
*	Value at the catastrophic disruption threshold
$'$	Oblique impact
†	Reverse impact onto the projectile in the hit-and-run regime
Subscripts	
targ	Target
p	Projectile
tot	Target + projectile
interact	Interacting fraction
α	Interacting projectile fraction
γ=1	Equal-mass collision
lr	Largest remnant
slr	Second largest remnant
rem	Fragments smaller than the largest remnant
core	Core fraction of a differentiated body
Constants	
ρ_1	Density of 1000 kg m^{-3}
G	Gravitational constant

A.1. A General Formulation for Collision Outcomes

We summarize the sequence of logic that should be applied to determine the dynamical outcome of any collision in the gravity regime using our analytic model. First, we identify the boundaries of the major collision regimes.

1. For a given collision scenario ($M_{\rm p}$, $M_{\rm targ}$, b, V_i, and $R_{\rm p}$ and $R_{\rm targ}$ from the bulk densities of the bodies), calculate the

Table 3
Sources and Description of Catastrophic Disruption Data Presented in Figures 4 and 12

Symbol	Target Description	Source
Weak targets		
▲, △	10 km PKDGRAV rubble piles	This work
+	1–50 km PKDGRAV rubble piles	Stewart & Leinhardt (2009)
★, open star	1 km PKDGRAV rubble piles	Leinhardt et al. (2000)
◀	weak 2–50 km basalt	Leinhardt & Stewart (2009)
•	hydrodynamic 2–50 km basalt	Leinhardt & Stewart (2009)
Hexagon	50 km ice	Leinhardt & Stewart (2009)
Strong targets		
*	1–100 km radius basalt	Benz & Asphaug (1999)
▼	2–50 km basalt	Leinhardt & Stewart (2009)
⊗	0.3–100 km microporous rock (pumice)	Jutzi et al. (2010)
⊠	0.3–100 km basalt	Jutzi et al. (2010)
⋈	10 km macroporous basalt	Benz (2000)
Hourglass	10 km basalt	Benz (2000)
Hydrodynamic planets		
◆, ◇	2.2 Mercury-mass bodies, differentiated rock and iron	Benz et al. (2007)
▶	0.4 and 7 Earth-mass bodies, pure rock	Marcus et al. (2009)
×	1–10 Earth-mass bodies, differentiated rock and iron	Marcus et al. (2009)
■, □	0.5–5 Earth-mass bodies, differentiated water and rock	Marcus et al. (2010b)

Notes. Filled and line symbols indicate head-on collisions ($b = 0$). Open symbols indicate oblique impacts: $b = 0.15, 0.3$ for open star, $0.35 < b < 0.9$ for △, $b = 0.5$ for □ and ◇, and $b = 0.71$ for ⋈, hourglass, hexagon, ⊗, and ⊠.

interacting mass fraction of the projectile, $m_{\rm interact} = \alpha M_{\rm p}$ (Equation (11)).

2. If $V_i < V'_{\rm esc}$ (Equation (53)), then the impact is in the *perfect merging regime*.
3. Calculate the critical impact parameter $b_{\rm crit}$ for the collision (Equation (6)). If $b < b_{\rm crit}$, then it is a non-grazing impact, else it is a grazing impact.
4. Calculate the catastrophic disruption criterion, $Q'^{*}_{\rm RD}$, and corresponding critical impact velocity, V'^{*}, for the specific impact scenario.
   (a) Calculate R_{C1} from the total mass and density of 1000 kg m^{-3}.
   (b) Calculate the principal disruption value for an equivalent equal-mass collision at R_{C1}, $Q^{*}_{{\rm RD},\gamma=1}$ (Equation (28)), and its corresponding critical impact velocity, $V^{*}_{\gamma=1}$ (Equation (30)), using the material parameter c^{*}.
   (c) Calculate the reduced mass, μ, and the reduced mass using the interacting mass, μ_α (Equation (12).)
   (d) Calculate the disruption criterion, $Q^{*}_{\rm RD}$, and critical impact velocity, V^{*}, for a head-on impact with the desired mass ratio, γ, using Equations (23) and (22) and the material parameter $\bar{\mu}$.
   (e) The value for the disruption energy, $Q'^{*}_{\rm RD}$, and critical impact velocity, $V'^{*}_{\rm RD}$, for the desired impact angle are found using Equations (15) and (16).
5. Calculate the value for Q_R required for onset of erosion, $M_{\rm lr} = M_{\rm targ}$, using the value of $Q'^{*}_{\rm RD}$ and the universal law for the mass of the largest remnant (Equation (5)). From this Q_R, derive the impact velocity for the onset of target erosion, $V_{\rm erosion}$, from Equation (1).
6. For grazing impacts ($b > b_{\rm crit}$), the *hit-and-run regime* is bounded by $V'_{\rm esc} < V_i < V_{\rm erosion}$. Note that the graze-and-merge regime is a subset of this range, but it is not explicitly defined in this work (see Genda et al. 2011b).
7. Calculate the value for Q_R required for the onset of super-catastrophic disruption, $M_{\rm lr} = 0.1 M_{\rm tot}$, using the value of $Q'^{*}_{\rm RD}$ and the universal law for the mass of the largest remnant (Equation (5)). From this Q_R, derive the impact velocity for the onset of super-catastrophic disruption, $V_{\rm supercat}$, from Equation (1).
8. For all impact angles, the target is eroded when $V_i > V_{\rm erosion}$ and the impact is in the *erosion regime*.
9. For all impact angles, the impact is in the *super-catastrophic disruption regime* when $V_i > V_{\rm supercat}$.
10. For non-grazing events and $V'_{\rm esc} < V_i < V_{\rm supercat}$, the impact is in the *disruption regime* and the universal law for the mass of the largest remnant applies. The partial *accretion regime* is bounded by $V'_{\rm esc} < V_i < V_{\rm erosion}$.
11. For grazing events and $V_{\rm erosion} < V_i < V_{\rm supercat}$, the impact is in the *disruption regime* and the universal law for the mass of the largest remnant applies only for $M_{\rm lr} < M_{\rm targ}$.
12. In the hit-and-run regime, calculate the critical disruption energy for the reverse impact onto the projectile, $Q'^{\dagger *}_{\rm RD}$, as described in Section 4.2, and its corresponding $V'^{\dagger *}$. Use Equations (5) or (44) to determine the largest remnant after disruption of the total mass involved in the reverse impact, $M_{\rm interact} + M_{\rm p}$.

In the *merging regime*, mass and momentum are conserved. In the *disruption regime*:

1. Determine the mass of the largest remnant $M_{\rm lr}$ from the universal law (Equation (5)) using Q_R and $Q'^{*}_{\rm RD}$.
2. Determine the mass of the second largest remnant $M_{\rm slr}$ using Equation (37) with $\beta = 2.85$, $N_1 = 1$, and $N_2 = 2$. The size distribution of the tail of smaller fragments is described by Equation (31).
3. For $b = 0$, assume that the largest remnant obtains the velocity of the center of mass; for $b > 0.7$ assume that the largest remnant maintains $V_{\rm targ}$. For $0 < b < 0.7$, the largest remnant velocity is some quasi-linear function of b.

Table 4
Summary of All Simulation Parameters and Results

$\frac{M_p}{M_{targ}}$	b	V_i (m s^{-1})	$\frac{M_{lr}}{M_{tot}}$	$\frac{M_{slr}}{M_{tot}}$	Q_R (J kg^{-1})
0.025	0.00	9	1.00	9.64e-05	9.69e-01
0.025	0.00	14	1.00	9.64e-05	2.34e+00
0.025	0.00	18	1.00	9.64e-05	3.88e+00
0.025	0.00	22	0.99	1.93e-04	5.79e+00
0.025	0.00	50	0.94	3.86e-04	2.99e+01
0.025	0.00	60	0.90	5.78e-04	4.31e+01
0.025	0.00	70	0.88	7.71e-04	5.86e+01
0.025	0.00	100	0.77	1.45e-03	1.20e+02
0.025	0.00	120	0.67	2.41e-03	1.72e+02
0.025	0.00	140	0.55	1.19e-02	2.34e+02
0.025	0.00	160	0.51	6.17e-03	3.06e+02
0.025	0.00	180	0.35	1.84e-02	3.88e+02
0.025	0.00	200	0.27	1.65e-02	4.79e+02
0.025	0.00	400	0.00	2.99e-03	1.91e+03
0.025	0.35	9	1.00	9.64e-05	9.69e−01
0.025	0.35	14	0.99	1.93e-04	2.34e+00
0.025	0.35	18	0.99	1.93e-04	3.88e+00
0.025	0.35	22	0.99	1.93e-04	5.79e+00
0.025	0.35	100	0.81	7.71e-04	1.20e+02
0.025	0.35	160	0.60	6.07e-03	3.06e+02
0.025	0.35	200	0.45	5.88e-03	4.79e+02
0.025	0.35	300	0.07	4.76e-02	1.08e+03
0.025	0.35	400	0.02	1.13e-02	1.91e+03
0.025	0.70	9	0.99	1.45e-03	9.69e−01
0.025	0.70	14	0.98	9.64e-04	2.34e+00
0.025	0.70	18	0.98	1.93e-04	3.88e+00
0.025	0.70	22	0.98	1.93e-04	5.79e+00
0.025	0.70	160	0.84	6.75e-04	3.06e+02
0.025	0.70	200	0.80	8.68e-04	4.79e+02
0.025	0.70	300	0.65	2.41e-03	1.08e+03
0.025	0.70	400	0.47	6.07e-03	1.91e+03
0.025	0.70	500	0.26	1.33e-02	2.99e+03
0.025	0.70	600	0.05	2.80e-02	4.31e+03
0.025	0.90	9	0.98	1.88e-02	9.69e−01
0.025	0.90	15	0.98	1.58e-02	2.69e+00
0.025	0.90	20	0.98	1.27e-02	4.79e+00
0.025	0.90	25	0.98	9.26e-03	7.48e+00
0.025	0.90	30	0.97	6.27e-03	1.08e+01
0.025	0.90	40	0.97	1.93e-03	1.91e+01
0.025	0.90	50	0.97	6.75e-04	2.99e+01
0.025	0.90	60	0.97	2.12e-03	4.31e+01
0.025	0.90	400	0.88	2.89e-04	1.91e+03
0.025	0.90	500	0.84	4.82e-04	2.99e+03
0.025	0.90	600	0.78	7.71e-04	4.31e+03
0.025	0.90	700	0.70	2.70e-03	5.86e+03
0.025	0.90	800	0.74	1.45e-03	7.66e+03
0.025	0.90	900	0.66	2.02e-03	9.69e+03
0.025	0.90	1000	0.36	2.80e-03	1.20e+04
0.10	0.00	9	1.00	8.99e-05	3.37e+00
0.10	0.00	15	0.99	1.80e-05	9.35e+00
0.10	0.00	20	0.97	1.80e-04	1.66e+01
0.10	0.00	25	0.94	8.09e-04	2.60e+01
0.10	0.00	30	0.90	7.19e-04	3.74e+01
0.10	0.00	40	0.79	1.35e-03	6.65e+01
0.10	0.00	50	0.67	2.61e-03	1.04e+02
0.10	0.00	65	0.41	1.44e-02	1.76e+02
0.10	0.00	80	0.14	3.44e-02	2.66e+02
0.10	0.35	9	1.00	1.71e-03	3.37e+00
0.10	0.35	15	0.96	1.08e-03	9.35e+00
0.10	0.35	20	0.93	1.89e-03	1.66e+01
0.10	0.35	25	0.90	1.44e-03	2.60e+01
0.10	0.35	30	0.87	1.44e-03	3.74e+01
0.10	0.35	40	0.79	1.98e-03	6.65e+01

Table 4
(Continued)

$\frac{M_p}{M_{targ}}$	b	V_i (m s^{-1})	$\frac{M_{lr}}{M_{tot}}$	$\frac{M_{slr}}{M_{tot}}$	Q_R (J kg^{-1})
0.10	0.35	50	0.72	1.89e-03	1.04e+02
0.10	0.35	65	0.62	5.13e-03	1.76e+02
0.10	0.35	80	0.47	5.85e-03	2.66e+02
0.10	0.35	100	0.33	1.16e-02	4.15e+02
0.10	0.70	9	0.95	4.76e-02	3.37e+00
0.10	0.70	15	0.92	3.72e-02	9.35e+00
0.10	0.70	20	0.90	3.43e-02	1.66e+01
0.10	0.70	25	0.90	1.42e-02	2.60e+01
0.10	0.70	30	0.89	8.63e-03	3.74e+01
0.10	0.70	40	0.87	2.07e-03	6.65e+01
0.10	0.70	50	0.86	1.53e-03	1.04e+02
0.10	0.70	100	0.77	2.16e-03	4.15e+02
0.10	0.70	150	0.63	1.53e-03	9.35e+02
0.10	0.70	200	0.52	3.51e-03	1.66e+03
0.10	0.70	300	0.21	1.15e-02	3.74e+03
0.10	0.90	9	0.92	8.21e-02	3.37e+00
0.10	0.90	15	0.91	8.44e-02	9.35e+00
0.10	0.90	20	0.91	8.21e-02	1.66e+01
0.10	0.90	25	0.91	8.21e-02	2.60e+01
0.10	0.90	30	0.91	7.85e-02	3.74e+01
0.10	0.90	40	0.91	7.68e-02	6.65e+01
0.10	0.90	50	0.91	6.83e-02	1.04e+02
0.10	0.90	60	0.90	6.43e-02	1.50e+02
0.10	0.90	70	0.90	6.09e-02	2.04e+02
0.10	0.90	80	0.90	5.96e-02	2.66e+02
0.10	0.90	100	0.90	1.71e-02	4.15e+02
0.10	0.90	120	0.89	2.88e-03	5.98e+02
0.10	0.90	140	0.88	2.07e-03	8.14e+02
0.10	0.90	300	0.84	4.50e-04	3.74e+03
0.10	0.90	400	0.70	6.29e-04	6.65e+03
0.10	0.90	500	0.61	1.80e-03	1.04e+04
0.10	0.90	600	0.57	4.77e-03	1.50e+04
0.10	0.90	700	0.53	2.07e-03	2.04e+04
0.10	0.90	800	0.55	2.16e-03	2.66e+04
0.10	0.90	900	0.57	7.19e-03	3.37e+04
0.25	0.00	9	1.00	7.89e-05	6.52e+00
0.25	0.00	14	0.98	1.58e-04	1.58e+01
0.25	0.00	18	0.94	3.95e-04	2.61e+01
0.25	0.00	22	0.88	1.66e-03	3.89e+01
0.25	0.00	30	0.69	6.55e-03	7.24e+01
0.25	0.00	40	0.40	1.95e-02	1.29e+02
0.25	0.00	50	0.09	1.66e-02	2.01e+02
0.25	0.00	60	0.01	1.07e-02	2.90e+02
0.25	0.35	14	0.93	1.40e-02	1.58e+01
0.25	0.35	18	0.84	1.89e-02	2.61e+01
0.25	0.35	22	0.78	9.00e-03	3.89e+01
0.25	0.35	30	0.67	5.29e-03	7.24e+01
0.25	0.35	40	0.53	6.31e-03	1.29e+02
0.25	0.35	45	0.46	5.52e-03	1.63e+02
0.25	0.35	50	0.37	4.97e-03	2.01e+02
0.25	0.35	55	0.33	1.71e-02	2.43e+02
0.25	0.35	60	0.25	7.42e-03	2.90e+02
0.25	0.35	65	0.17	2.36e-02	3.40e+02
0.25	0.35	80	0.07	1.12e-02	5.15e+02
0.25	0.35	9	1.00	1.89e-03	6.52e+00
0.25	0.70	9	0.84	1.55e-01	6.52e+00
0.25	0.70	14	0.81	1.54e-01	1.58e+01
0.25	0.70	18	0.79	1.36e-01	2.61e+01
0.25	0.70	22	0.78	1.18e-01	3.89e+01
0.25	0.70	27	0.77	1.02e-01	5.86e+01
0.25	0.70	36	0.74	5.44e-02	1.04e+02
0.25	0.70	50	0.69	5.84e-03	2.01e+02
0.25	0.70	60	0.66	6.16e-03	2.90e+02

Table 4
(Continued)

$\frac{M_p}{M_{targ}}$	b	V_i (m s^{-1})	$\frac{M_{lr}}{M_{tot}}$	$\frac{M_{slr}}{M_{tot}}$	Q_R (J kg^{-1})
0.25	0.70	70	0.64	2.05e-03	3.94e+02
0.25	0.70	80	0.58	1.42e-03	5.15e+02
0.25	0.70	100	0.52	3.79e-03	8.04e+02
0.25	0.70	125	0.42	3.79e-03	1.26e+03
0.25	0.70	150	0.32	5.21e-03	1.81e+03
0.25	0.70	175	0.10	7.89e-05	2.46e+03
0.25	0.90	9	0.81	1.91e-01	6.52e+00
0.25	0.90	14	0.80	1.93e-01	1.58e+01
0.25	0.90	18	0.80	1.90e-01	2.61e+01
0.25	0.90	22	0.80	1.88e-01	3.89e+01
0.25	0.90	27	0.79	1.87e-01	5.86e+01
0.25	0.90	36	0.79	1.74e-01	1.04e+02
0.25	0.90	50	0.79	1.87e-01	2.01e+02
0.25	0.90	60	0.79	1.87e-01	2.90e+02
0.25	0.90	70	0.79	1.83e-01	3.94e+02
0.25	0.90	100	0.79	1.62e-01	8.04e+02
0.25	0.90	120	0.77	1.44e-01	1.16e+03
0.25	0.90	150	0.73	5.26e-02	1.81e+03
0.25	0.90	200	0.67	3.63e-03	3.22e+03
0.25	0.90	250	0.61	1.34e-03	5.03e+03
0.25	0.90	300	0.55	1.10e-03	7.24e+03
0.25	0.90	350	0.47	3.39e-03	9.85e+03
0.25	0.90	400	0.42	4.02e-03	1.29e+04
0.25	0.90	450	0.31	5.84e-03	1.63e+04
1.00	0.00	15	0.97	2.46e-04	2.83e+01
1.00	0.00	18	0.93	4.42e-04	4.07e+01
1.00	0.00	24	0.76	3.66e-03	7.24e+01
1.00	0.00	24	0.76	2.72e-03	7.24e+01
1.00	0.00	24	0.77	3.06e-03	7.24e+01
1.00	0.00	30	0.50	1.06e-02	1.13e+02
1.00	0.00	30	0.49	1.04e-02	1.13e+02
1.00	0.00	30	0.47	1.23e-02	1.13e+02
1.00	0.00	35	0.12	5.47e-02	1.54e+02
1.00	0.00	35	0.12	3.76e-02	1.54e+02
1.00	0.00	35	0.14	3.01e-02	1.54e+02
1.00	0.00	38	0.05	2.77e-02	1.81e+02
1.00	0.00	38	0.04	3.86e-02	1.81e+02
1.00	0.00	38	0.03	2.07e-02	1.81e+02
1.00	0.35	15	0.98	3.93e-04	2.83e+01
1.00	0.35	16	0.97	2.95e-04	3.22e+01
1.00	0.35	17	0.48	4.56e-01	3.63e+01
1.00	0.35	18	0.47	4.46e-01	4.07e+01
1.00	0.35	30	0.23	1.98e-01	1.13e+02
1.00	0.35	45	0.02	1.22e-02	2.55e+02
1.00	0.70	8	1.00	0.00e+00	8.04e+00
1.00	0.70	10	0.50	4.97e-01	1.26e+01
1.00	0.70	11	0.50	4.97e-01	1.52e+01
1.00	0.70	12	0.50	4.93e-01	1.81e+01
1.00	0.70	13	0.50	4.95e-01	2.12e+01
1.00	0.70	14	0.50	4.89e-01	2.46e+01
1.00	0.70	30	0.44	4.41e-01	1.13e+02
1.00	0.70	50	0.39	3.82e-01	3.14e+02
1.00	0.70	80	0.28	2.74e-01	8.04e+02
1.00	0.70	150	0.04	1.05e-02	2.83e+03
1.00	0.90	7	1.00	4.97e-01	6.16e+00
1.00	0.90	15	0.50	4.95e-01	2.83e+01
1.00	0.90	20	0.50	4.95e-01	5.03e+01
1.00	0.90	40	0.50	4.90e-01	2.01e+02
1.00	0.90	100	0.48	4.80e-01	1.26e+03
1.00	0.90	200	0.44	4.30e-01	5.03e+03
1.00	0.90	300	0.41	4.06e-01	1.13e+04
1.00	0.90	400	0.35	3.39e-01	2.01e+04
1.00	0.90	600	0.26	2.51e-01	4.52e+04

4. The mass-velocity distribution of the smaller fragments with respect to the largest remnant is given by Equation (39).

In the *super-catastrophic disruption regime*:

1. Determine the mass of the largest remnant M_{lr} from the power law (Equation (44)) using Q_R and Q'^{*}_{RD} (Equation (15)).
2. The size and velocity distributions of the fragments with respect to the largest remnant are the same as in the disruption regime.

In the *hit-and-run regime*:

1. The mass of the largest remnant M_{lr} is approximately equal to the target mass M_{targ}.
2. The mass of the second largest remnant M_{slr} is estimated using the universal law and disruption criteria for the reverse impact on the projectile, $Q'^{\dagger *}_{RD}$.
3. When the projectile is disrupted, the size and velocity distributions of the fragments are described as in the disruption regime with respect to the largest remnant from the projectile.
4. In the special case of $\gamma \sim 1$, the onset of erosion occurs simultaneously in both bodies and $M_{lr} \sim M_{slr}$. Then, use $N_1 = 2$ and $N_2 = 4$ to calculate the size distribution. One can assume that the fragments from both the projectile and target have identical size and velocity distributions with respect to their body of origin.

In the disruption and super-catastrophic disruption regimes, a differentiated target may change its bulk composition by stripping off a portion of the mantle. Bulk compositional changes may be tracked using the results from Marcus et al. (2010b). They found that the core mass fraction after a disruptive collision falls between two idealized models, and we suggest using an average of these two results.

1. Model 1—cores always merge: given the original $M_{core,targ}$ and $M_{core,p}$, the post-impact core is $M_{core} = \min(M_{lr}, M_{core,targ} + M_{core,p})$.
2. Model 2—cores only merge on accretion: when $M_{lr} > M_{targ}$, $M_{core} = M_{core,targ} + \min(M_{core,p}, M_{lr} - M_{targ})$. When $M_{lr} < M_{targ}$, assume that none of the projectile accretes and the mantle is stripped first. Then, $M_{core} = \min(M_{core,targ}, M_{lr})$.

In hit-and-run events with projectile disruption, the same relations may be used to estimate the bulk changes in composition for the projectile.

Finally, Housen & Holsapple (2011) provide scaling laws for the gravitationally escaping ejecta from the target in the impact cratering regime. The impact cratering regime occurs at the low-velocity end of the disruption regime, when $V_i > V'_{esc}$, $M_p \ll M_{targ}$, and $M_{lr} \sim M_{targ}$. Based on many laboratory experiments, Housen & Holsapple (2011) find that approximately $0.01 M_p$ achieves escape velocity in cratering events of $V_i \sim V_{esc}$ (see their Figure 16). In addition, Svetov (2011) provides empirical equations for ejected material in cratering collisions on self-gravitating bodies.

REFERENCES

Agnor, C., & Asphaug, E. 2004a, ApJ, 613, L157
Agnor, C., & Asphaug, E. 2004b, Eos Trans. AGU, 85 (47), AGU Fall Meeting Abstract P32A-02
Agnor, C. B., Canup, R. M., & Levison, H. F. 1999, Icarus, 142, 219

Alibert, Y., Mordasini, C., & Benz, W. 2011, A&A, 526, A63
Asphaug, E. 2009, Annu. Rev. Earth Planet. Sci., 37, 413
Asphaug, E. 2010, Chem. Erde/Geochem., 70, 199
Asphaug, E., Agnor, C. B., & Williams, Q. 2006, Nature, 439, 155
Batalha, N. M., Borucki, W. J., Bryson, S. T., et al. 2011, ApJ, 729, 27
Beauge, C., & Aarseth, S. J. 1990, MNRAS, 245, 30
Benz, W. 2000, Space Sci. Rev., 92, 279
Benz, W., Anic, A., Horner, J., & Whitby, J. A. 2007, Space Sci. Rev., 132, 189
Benz, W., & Asphaug, E. 1994, Icarus, 107, 98
Benz, W., & Asphaug, E. 1999, Icarus, 142, 5
Benz, W., Slattery, W. L., & Cameron, A. G. W. 1988, Icarus, 74, 516
Borucki, W. J., Koch, D. G., Basri, G., et al. 2011, ApJ, 736, 19
Bottke, W. F., Durda, D. D., Nesvorný, D., et al. 2005, Icarus, 175, 111
Bottke, W. F., Jr., Vokrouhlický, D., Rubincam, D. P., & Broz, M. 2002, in Asteroids III, ed. W. F. Bottke, Jr., A. Cellino, P. Paolicchi, & R. P. Binzel (Tucson, AZ: Univ. Arizona Press), 395
Canup, R. M. 2004, Icarus, 168, 433
Canup, R. M. 2005, Science, 307, 546
Canup, R. M. 2008, Icarus, 196, 518
Chambers, J. E. 2001, Icarus, 152, 205
Chau, K. T., Wong, R. H. C., & Wu, J. J. 2002, Int. J. Rock Mech. Min. Sci., 39, 69
Cuzzi, J. N., Hogan, R. C., & Shariff, K. 2008, ApJ, 687, 1432
Davis, D. R., Chapman, C. R., Greenberg, R., Weidenschilling, S. J., & Harris, A. W. 1979, in Asteroids, ed. T. Gehrels (Tucson, AZ: Univ. Arizona Press), 528
Durda, D. D., Bottke, W. F., Enke, B. L., et al. 2004, Icarus, 170, 243
Durda, D. D., Bottke, W. F., Nesvorný, D., et al. 2007, Icarus, 186, 498
Fujiwara, A., Kamimoto, G., & Tsukamoto, A. 1977, Icarus, 31, 277
Genda, H., Kokubo, E., & Ida, S. 2011a, in 42nd Lunar and Planetary Science Conference, March 7–11, The Woodlands, TX (Houston, TX: Lunar and Planetary Institute), LPI Contribution No. 1608 Abs., 2090
Genda, H., Kokubo, E., & Ida, S. 2011b, ApJ, in press (arXiv:1109.4330)
Holsapple, K., Giblin, I., Housen, K., Nakamura, A., & Ryan, E. 2002, in Asteroids III, ed. W. F. Bottke, Jr., A. Cellino, P. Paolicchi, & R. P. Binzel (Tucson, AZ: Univ. Arizona Press), 443
Holsapple, K. A. 1993, Annu. Rev. Earth Planet. Sci., 21, 333
Holsapple, K. A., & Schmidt, R. M. 1987, J. Geophys. Res., 92, 6350
Housen, K. R., & Holsapple, K. A. 1990, Icarus, 84, 226
Housen, K. R., & Holsapple, K. A. 1999, Icarus, 142, 21
Housen, K. R., & Holsapple, K. A. 2011, Icarus, 211, 856
Howard, A. W., Marcy, G. W., Bryson, S. T., et al. 2011, ApJ, submitted (arXiv:1103.2541)
Howard, A. W., Marcy, G. W., Johnson, J. A., et al. 2010, Science, 330, 653
Ida, S., & Lin, D. N. C. 2010, ApJ, 719, 810
Johansen, A., Oishi, J. S., Mac Low, M.-M., et al. 2007, Nature, 448, 1022
Jutzi, M., Michel, P., Benz, W., & Richardson, D. C. 2010, Icarus, 207, 54
Kato, M., Iijima, Y., Arakawa, M., et al. 1995, Icarus, 113, 423
Kato, M., Iojoma, Y., Okimuar, Y., et al. 1992, Physics and Chemistry of Ice (Sapporo: Hokkaido Univ. Press), 464
Kenyon, S. J., & Bromley, B. C. 2008, ApJS, 179, 451
Kenyon, S. J., & Bromley, B. C. 2009, ApJ, 690, L140
Kenyon, S. J., Bromley, B. C., O'Brien, D. P., & Davis, D. R. 2008, in The Solar System Beyond Neptune, ed. M. A. Barucci, H. Boehnhardt, D. P. Cruikshank, & A. Morbidelli (Tucson, AZ: Univ. Arizona Press), 293
Kobayashi, H., Tanaka, H., & Krivov, A. V. 2011, ApJ, 738, 35
Kokubo, E., & Genda, H. 2010, ApJ, 714, L21
Kokubo, E., & Ida, S. 2002, ApJ, 581, 666
Korycansky, D. G., & Asphaug, E. 2009, Icarus, 204, 316
Leinhardt, Z. M., Marcus, R. A., & Stewart, S. T. 2010, ApJ, 714, 1789
Leinhardt, Z. M., & Richardson, D. C. 2002, Icarus, 159, 306
Leinhardt, Z. M., & Richardson, D. C. 2005, Icarus, 176, 432
Leinhardt, Z. M., Richardson, D. C., Lufkin, G., & Haseltine, J. 2009, MNRAS, 396, 718
Leinhardt, Z. M., Richardson, D. C., & Quinn, T. 2000, Icarus, 146, 133
Leinhardt, Z. M., & Stewart, S. T. 2009, Icarus, 199, 542
Lissauer, J. J. 1993, ARA&A, 31, 129
Marcus, R. A., Sasselov, D., Hernquist, L., & Stewart, S. T. 2010a, ApJ, 712, L73
Marcus, R. A., Sasselov, D., Stewart, S. T., & Hernquist, L. 2010b, ApJ, 719, L45
Marcus, R. A., Stewart, S. T., Sasselov, D., & Hernquist, L. 2009, ApJ, 700, L118
Matsui, T., Waza, T., Kani, K., & Suzuki, S. 1982, J. Geophys. Res., 87, 10968
Melosh, H. J., & Ryan, E. V. 1997, Icarus, 129, 562
Michel, P., Benz, W., Tanga, P., & Richardson, D. C. 2001, Science, 294, 1696
Michel, P., Tanga, P., Benz, W., & Richardson, D. C. 2002, Icarus, 160, 10
Morbidelli, A. 2010, C. R. Phys., 11, 651
Morbidelli, A., Bottke, W. F., Nesvorný, D., & Levison, H. F. 2009, Icarus, 204, 558
Morbidelli, A., Levison, H. F., & Gomes, R. 2008, in The Solar System Beyond Neptune, ed. M. A. Barucci, H. Boehnhardt, D. P. Cruikshank, & A. Morbidelli (Tucson, AZ: Univ. Arizona Press), 275
Mordasini, C., Alibert, Y., & Benz, W. 2009, A&A, 501, 1139
Nagasawa, M., Lin, D. N. C., & Thommes, E. 2005, ApJ, 635, 578
Nesvorný, D., Bottke, W. F., Levison, H. F., & Dones, L. 2003, ApJ, 591, 486
Nesvorný, D., Enke, B. L., Bottke, W. F., et al. 2006, Icarus, 183, 296
Nesvorný, D., Ferraz-Mello, S., Holman, M., & Morbidelli, A. 2002, in Asteroids III, ed. W. F. Bottke, Jr., A. Cellino, P. Paolicchi, & R. P. Binzel (Tucson, AZ: Univ. Arizona Press), 379
Richardson, D. C., Leinhardt, Z. M., Melosh, H. J., Bottke, W. F., Jr., & Asphaug, E. 2002, in Asteroids III, ed. W. F. Bottke, Jr., A. Cellino, P. Paolicchi, & R. P. Binzel (Tucson, AZ: Univ. Arizona Press), 501
Schlaufman, K. C., Lin, D. N. C., & Ida, S. 2010, ApJ, 724, L53
Senft, L. E., & Stewart, S. T. 2009, Earth Planet. Sci. Lett., 287, 471
Shoemaker, E. M. 1962, in Physics and Astronomy of the Moon, ed. Z. Kopal (New York: Academic), 283
Stadel, J. G. 2001, PhD thesis, Univ. Washington
Stewart, S. T., & Leinhardt, Z. M. 2009, ApJ, 691, L133
Stewart, S. T., & Leinhardt, Z. M. 2011, ApJ, submitted (arXiv:1109.4588)
Svetov, V. 2011, Icarus, 214, 316
Walsh, K. J., Morbidelli, A., Raymond, S. N., O'Brien, D. P., & Mandell, A. M. 2011, Nature, 475, 206
Weidenschilling, S. J. 2011, Icarus, 214, 671
Winn, J. N., Matthews, J. M., Dawson, R. I., et al. 2011, ApJ, 737, L18
Wyatt, M. C., & Dent, W. R. F. 2002, MNRAS, 334, 589